HIGH POWER mm-WAVE TUNEABLE REFLECTIVE TERMINATIONS

A thesis presented for the degree of Doctor of Philosophy

by

SEYED URMAN GHOZATI

This work was awarded a PhD on a posthumous basis and is likely to contain typographical or grammatical errors or may under normal circumstances have had additional editing prior to publication

supervised by

Dr. Roberto Quaglia

Dr. Jonathan Lees

Centre for High Frequency Engineering

School of Engineering

Cardiff University

United Kingdom

2024

ABSTRACT

A Ka-band single pole double throw (SPDT) switch capable of operating at power levels up to 3 W, along with its corresponding behavioural model, was developed to demonstrate the application of tunable reflective terminations within an orthogonal load modulated balanced amplifier (OLMBA) architecture, enabling the dynamic selection of reactive loads.

To determine the most suitable switching cell for the target frequency band and operating conditions, the investigation began with an analysis of high electron mobility transistor (HEMT)-structured GaN-on-SiC with 150 nm and 120 nm gate length technologies across different device peripheries, achieved by varying gate width and number of gate fingers. Standard small- and large-signal characterisation were conducted to assess the frequency response and power-handling capabilities. Additionally, load-pull (LP) measurements were performed to capture the device behaviour under non-50 Ω conditions, providing insights into realistic operational scenarios.

The acquired data was used to develop the first Cardiff behavioural model for microwave switches, paving the way for further refinements on future models and optimisations of the tunable reflective termination application. Experimental findings highlight the significant impact of device periphery scaling on power-handling performance, with larger periphery devices exhibiting minimal gain compression at elevated power levels. Moreover, isolation characteristics in the off-state were found to be predominantly influenced by the applied bias voltage, with higher voltages delivering enhanced isolation.

Subsequently, the Ka-band SPDT was designed and developed, incorporating a previously shortlisted and characterised HEMT device. During the characterisation of the switching cells, it was observed that in the OFF state, the impedance deviates significantly,

shifting from a high impedance condition (approaching an open circuit) at lower frequencies to approximately ($\approx (0.121 - j0.655)Z_0$) near 30.5 GHz. To mitigate this degradation in performance at higher frequencies, an impedance transformation technique was implemented in the passive network design, ensuring improved frequency response. The fabricated SPDT exhibited an insertion loss of -1.8 dB and isolation exceeding -25 dB, while maintaining linearity up to 3 W at the centre frequency of 30.5 GHz. These performance metrics demonstrate the designed SPDT's viability for conventional applications, such as transceiver (TxRx) switching.

Finally, the designed SPDT was characterised through LP measurements to obtain the necessary data for the final phase of this study—the development of a behavioural model for the tunable reflective termination. The model was further enhanced to provide high accuracy with minimised data through an experimentally structured phase-distributed technique. This model was intended for implementation in computer-aided design (CAD) software, such as advanced design systems (ADS), to facilitate the efficient and effective design of the OLMBA architecture.

ACKNOWLEDGMENT

I would like to express my most heartfelt gratitude to;

Dr. Roberto Quaglia, without whose supervision this research would have been impossible. I have been privileged to benefit from his extensive knowledge, guidance, and support throughout my academic journey. He has taught me a legacy of hard work, honesty and kindness toward others. He demonstrated remarkable patience, teaching me that with perseverance and the right tools, any challenge can be overcome. I am grateful for the opportunity to work with and learn from such a remarkable character. I would also like to take this opportunity to wish him and his lovely family endless happiness.

Dr. Jonathan Lees, my second supervisor, from whom I have learnt immensely in both technical and professional aspects. His valuable feedback has been irreplaceable. He guided me in the right direction when I needed it, and inspired me in finding the best solutions to the biggest challenges. I am deeply thankful for all the support he has provided, from the very beginning up to shaping my professional career.

Dr. Kauser Chaudhury, Professor Paul Tasker, Professor Steve Cripps, Dr Aleksander Bogusz, and all other academic members of the CHFE group at Cardiff University for their invaluable support and guidance throughout my research.

The members of the EPSRC Centre for Doctoral Training in Compound Semiconductor Manufacturing at Cardiff University, particularly Professor Peter Smowton, Terri Delahunty, Dr. Daryl Beggs, Dr. Bo Hou, and Sarah Brasher, for providing me with this opportunity, facilitating my research journey, and their invaluable support throughout my research.

My amazing PhD colleagues—Ehsan (now Dr. Azad), Alex (now Dr. Baddeley), Wesley (now Dr. Sampson), Timmy (now Dr. Tian), Derek (now Dr Kozel), Aquila, JB, and Indy (soon to be Drs). We worked together, learnt from one another, supported each

other through challenges, and, most importantly, shared many memorable moments that made this journey so much easier. Thank you all for being there and for the good times we created along the way.

Ma, I saved the last one for you. No fancy words are needed—this was always for you. You wanted me to do it, and I did it, Ma.

Ma, you once said my old pain would fade one day
But you never said new ones would come my way
I waited for peace, but the silence just screamed
And healing felt further than I ever dreamed
The pain didn't leave—it just changed its face
New battles arrived, taking the old one's place
They broke me, Ma — they shattered me into pieces
They broke my mind, the place where peace is
But my pieces are brave; they refuse to flee
Each one searching, rebuilding me
Through all the noise, I still hear your tone
Saying " to moavafagh mishi, urman jonam sabr kon"
We'll meet again one sunny day beneath a blue sky
And I'll still be your little boy—just with a few more scars
urman 30/03/2025

PUBLICATIONS

- **Seyed Urman Ghozati**, E. Azad, K. Chaudhry, R. Quaglia, P. Tasker, "Cardiff Behavioral Model of a Ka-Band SPDT Switch Trained on Structured Minimization of Load-Pull Characterization Data," The International Workshop on Integrated Nonlinear Microwave and Millimetre-wave Circuits, Torino, Italy, 2025. In press.

- **Seyed Urman Ghozati**, R. Quaglia, "Ka-Band Single-Pole Double-Throw Switch in GaN MMIC Technology," International Journal of Microwave and Wireless Technologies, 2025, Cambridge University Press, Cambridge, United Kingdom, 2025. DOI:10.1017/S1759078725000108

- **Seyed Urman Ghozati**, A. Baddeley and R. Quaglia, "Large-signal characterization and behavioral modeling of mm-wave GaN HEMT switches tailored for advanced power amplifier architectures," 2024 IEEE Topical Conference on RF/Microwave Power Amplifiers for Radio and Wireless Applications (PAWR), San Antonio, TX, USA, 2024, pp. 21-23. DOI:10.1109/PAWR59907.2024.10438592

- **Seyed Urman Ghozati**, R. Quaglia, E. Azad, J. Powell, P. Tasker and S. Cripps, "Load Pull-Driven Behavioral Modelling of Microwave Switches for the Design of Tunable Reflective Terminations," 2023 18th European Microwave Integrated Circuits Conference (EuMIC), Berlin, Germany, 2023, pp. 1-4. DOI:10.23919/EuMIC58042.2023.10289021

OTHER CONTRIBUTIONS

- A. Varghese, A. Eblabla, Z. Wu, **Seyed Urman Ghozati** and K. Elgaid, "GaN-HEMT on Si as a Robust Visible-Blind UV Detector With High Responsivity," IEEE Sensors Journal, vol. 22, no. 12, pp. 12307-12313, 15 June15, 2022. DOI:10.1109/JSEN.2022.3170653

ABBREVIATIONS

RF radio frequency

RFPA radio frequency power amplifier

PA power amplifier

DPA Doherty power amplifier

LMBA load modulated balanced amplifier

OLMBA orthogonal load modulated balanced amplifier

CSP control signal power

Tx transmitter

Rx receiver

TxRx transceiver

mm-wave millimetre wave

MW microwave

S-band 2-4 GHz

Ka-band 27-40 GHz

FET field effect transistor

MESFET metal semiconductor field effect transistor

HEMT high electron mobility transistor

2DEG two dimensional electron gas

epilayers epitaxial layers

MS microwave switch

STPS switch-type phase shifter

PIN positive-intrinsic-negative

DIP dual in-line package

SPST single pole single throw

SPDT single pole double throw

DPDT double pole double throw

MT multiple throw

MEMS microelectromechanical systems

MAM metal-air-metal

MIM metal-insulator-metal

GaN gallium nitride

SiC silicon carbide

AlGaAs aluminium gallium arsenide

GaAs gallium arsenide

InAlAs indium aluminium arsenide

InGaAs indium gallium arsenide

MMIC monolithic microwave integrated circuits

PCB printed circuit board

IC integrated circuits

CAD computer aided design

ADS advanced design system (by Keysight)

PDK process design kit

EMT electromechanical tuner

ETS electronic tuner

DUT device under test

FOM figure of merit

LP load-pull

PNA precision network analyser

AM amplitude modulation

PM phase modulation

PNA-X precision network analyser extended

LSNA large signal network analyser

VNA vector network analyser

NVNA nonlinear vector network analyzer

GSG ground signal ground

TRL Thru-Reflect-Line

TRM Thru-Reflect-Matched

IMN input matching network

S-parameter scattering parameter

X-parameter non-linear network parameter

IL insertion loss

PBO power back-off

CW continuous wave

EM electro-magnetic

PHD poly-harmonics distortion

DWLUT direct wave look up table

NMSE normalised mean squared error

CHFE centre for high frequency engineering

TRH translational research hub

SYMBOLS

jX	reactive component
F_c	cut-off frequency
R_{on}	on-state channel resistance
C_{off}	off-state channel capacitance
R_{ds}	drain to source resistance
C_{ds}	drain to source capacitance
Z_{TH}	total high (off-state) impedance
Z_{TL}	total low (on-state) impedance
L_{ch}	channel inductance
X_L	inductive reactance
X_C	capacitive reactance
C	capacitance
L	inductance
Z_0	characteristics impedance
R_0	resistive impedance equal to source impedance
Z_S	source impedance

Z_L	load impedance
Z_T	total impedance
V_0	source voltage
V	total voltage
I	total current
V_i	voltage at port i
I_i	current at port i
I_1	current wave at the input port
I_2	current wave at the output port
V_1	voltage at input reference plane
V_2	voltage at output reference plane
a_n	incident wave at port n
b_n	reflected wave at port n
a_1	incident power wave at port 1
b_1	reflected power wave at port 1
a_2	incident power wave at port 2
b_2	reflected power wave at port 2
a_i	incident power wave at port i
b_i	reflected power wave at port i
a_i	incident power waves
b_i	reflected power waves

A	incident power wave amplitude
B	reflected power wave amplitude
A_1	incident travelling wave at port 1
A_2	reflected travelling wave at port 2
$A_{2,h}$	reflected travelling wave at port 2 for h order of the fundamental frequency
A_{11}	incident travelling wave at port 1 at fundamental frequency
A_{21}	incident travelling wave at port 2 at fundamental frequency
B_1	reflected travelling wave at port 1
B_2	incident travelling wave at port 2
$B_{2,h}$	incident travelling wave at port 2 for h order of the fundamental frequency
S	scattering matrix (network response function)
S_{21}	forward transmission coefficient
S_{11}	input reflection coefficient
S_{12}	reverse transmission coefficient
S_{22}	output reflection coefficient
Γ	complex reflection coefficient
Γ_{IN}	input reflection coefficient
Γ_{Out}	output reflection coefficient
Γ_S	source reflection coefficient
Γ_L	load reflection coefficient
$\Gamma_{L,h}$	complex load reflection coefficient at harmonics

RF_{in}	RF input port/signal
R_g	gate circuitry resistor
Z_R	reference Impedance
Z_R^*	conjugate of reference impedance
R_R	real part of reference impedance
X_R	imaginary part of reference impedance
P_{avs}	power available at source
P_L	power delivered to the load
P_{IN}	input Power
P_{OUT}	output Power
G_P	power gain or operating gain
G_T	transducer gain
PAE	power added efficiency
DC	direct current
f	frequency
F_0	fundamental frequency
$2F_0$	second harmonic
$3F_0$	third harmonic
h	number of harmonics
p	port number
F	describing function

G closed-loop active load load pull gain

3F50 3 gate-fingers configuration with 50 µm of gate width

3F100 3 gate-fingers configuration with 100 µm of gate width

5F50 5 gate-fingers configuration with 50 µm of gate width

5F100 5 gate-fingers configuration with 100 µm of gate width

7F50 7 gate-fingers configuration with 50 µm of gate width

7F100 7 gate-fingers configuration with 100 µm of gate width

9F50 9 gate-fingers configuration with 50 µm of gate width

9F100 9 gate-fingers configuration with 100 µm of gate width

a_j incident small signal wave at port j

f_s small signal frequency

f_{large} large signal frequency

f_c large signal tone

$S(fs)$ Hot S-parameters

S_{ij} scattering parameters

SI international system of units

V voltage

W watt (power unit)

k kilo

mm millimetre

µm micrometre

nm	nanometre
GHz	gigahertz
MHz	megahertz
dB	decibel
dBm	decibel-milliwatts
Ω	the SI unit of electrical resistance
pF	pico-Farad (10^{-12}F)
fF	femto-Farad (10^{-15}F)
π	3.14159265358979323846264338327950288419 7

List of Contents

List of Figures

LIST OF TABLES

CHAPTER 1

INTRODUCTION

In the ongoing pursuit of enhancing the efficiency and linearity of radio frequency power amplifiers (RFPA), advanced architectures have been devised to address the inherent limitations of traditional power amplifier designs. Among these, Doherty power amplifier (DPA) has emerged as a widely adopted approach that takes advantage of active load modulation to enhance efficiency under modulated signal excitation [1, 2]. Despite its advantages, conventional RFPA architectures, including balanced power amplifiers (PA), are inherently constrained by their fixed tuning networks. These fixed matching structures impose limitations on bandwidth and introduce efficiency degradation due to phase and amplitude imbalances stemming from coupler losses. Various solutions have been proposed to extend the bandwidth of DPAs, such as the implementation of non-linear passive element load modulation techniques [3]. However, these approaches often result in a trade-off, where the impedance presented to the output devices must be carefully optimised to balance performance across frequency, particularly in broadband applications like electronic warfare, where wide frequency coverage and high efficiency are simultaneously required. This highlights the necessity for alternative architectures capable of achieving optimal load modulation while maintaining high efficiency over a broad frequency range.

Consequently, the load modulated balanced amplifier (LMBA), introduced in [4], builds upon the foundation of a conventional balanced amplifier while incorporating a control signal power (CSP) at the output to sustain high power back-off (PBO) efficiency

across wideband applications. The core principle of the LMBA is to replace traditional passive matching networks with an active impedance tuning mechanism, achieved through CSP in conjunction with dynamic amplitude and phase control. By injecting a phase-synchronised "control signal" into the otherwise isolated output port, the impedance seen by the balanced transistors can be actively modulated across a broad resistive and reactive range. Interestingly, the modulation remains identical for each transistor, and the power injected through the CSP is fully recovered at the main output port, ensuring minimal efficiency loss while maintaining optimal performance over an extended frequency range.

While the LMBA has demonstrated both theoretical and practical advantages, its success has stimulated further exploration into similar architectures. A notable advancement in this evolution is the OLMBA, introduced in [5]. Unlike the LMBA, where the CSP directly modulates the impedance at the output, the OLMBA modifies the architecture by combining the CSP buffer signal with the main radio frequency (RF) signal at the input of the first balanced stage. The previously hosted CSP at the output is now terminated with a reactive component, "jX", significantly reducing the power requirements for the CSP, thereby improving efficiency and easing implementation constraints. However, unlike the symmetric load modulation of the LMBA, the OLMBA introduces an asymmetric load variation, leading to a more intricate interaction between the amplifier's active devices. This results in a complex system response, necessitating extensive non-linear simulations to achieve an optimal design. Figure 1.1 illustrates the architectural evolution of the OLMBA from a conventional balanced PA.

While it has been demonstrated that the OLMBA offers significant practical performance enhancements [6], the optimal value of jX is not universally fixed and varies depending on the specific amplifier design and operating conditions. This inherent variability poses a significant challenge, motivating our investigation into potential solutions to address this issue.

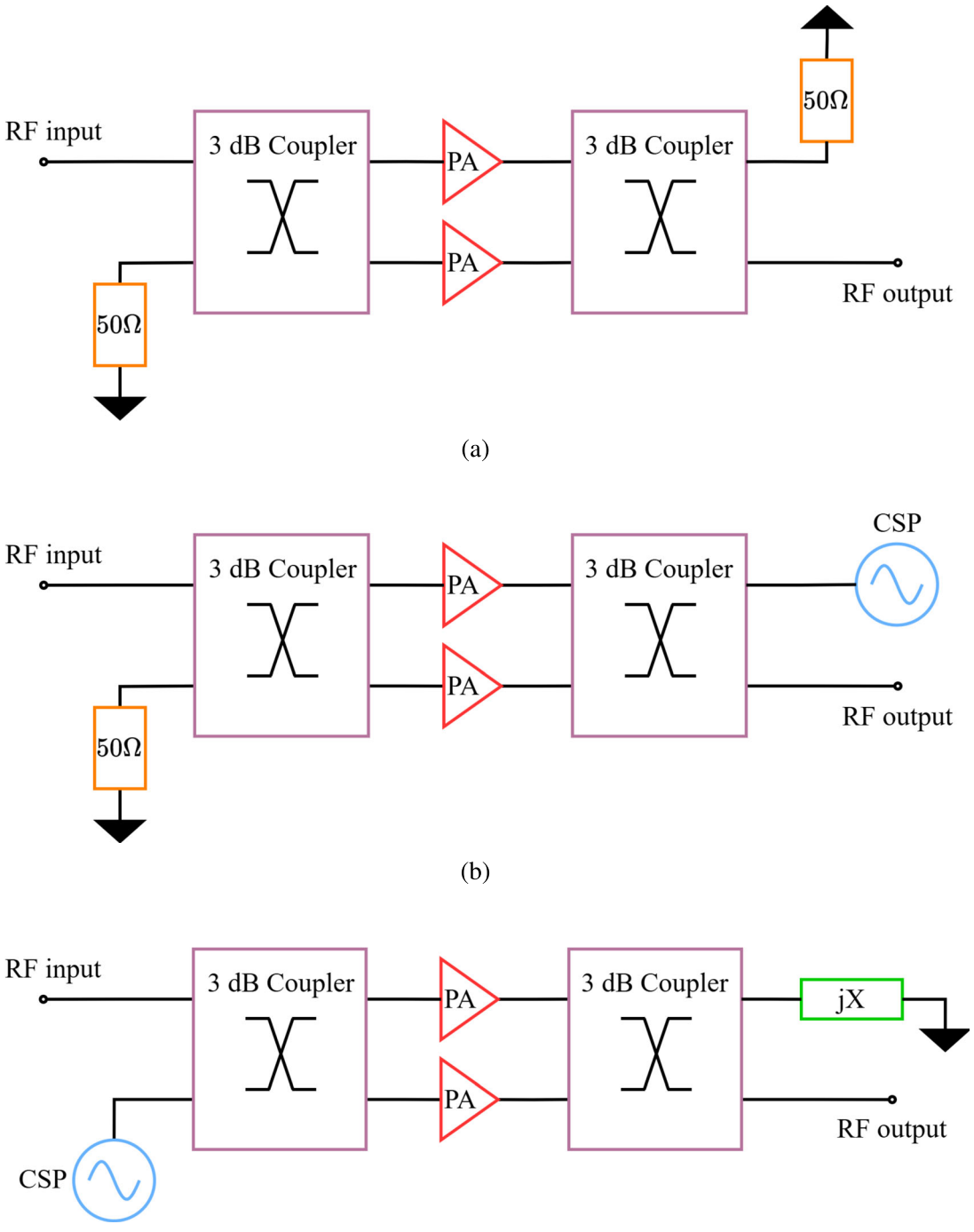

Figure 1.1: Evolution of the active load modulation architectures from Balanced PA (a), to LMBA (b), and OLMBA (c).

1.1 MOTIVATION

It has been established that the optimal jX value is not fixed and varies based on the specific design and operating conditions of the OLMBA. To date, no theoretical or mathematical framework exists that allows for an accurate pre-design estimation of jX. This variability introduces a fundamental challenge in achieving optimal performance without extensive post-fabrication tuning.

Ensuring the selection of an appropriate jX typically requires an extensive number of iterative evaluations, where different reactive terminations are manually introduced into the OLMBA after fabrication. However, as the number of required iterations increases, the manual tuning approach becomes impractical and inefficient. This underscores the necessity for an electronically controlled switching network capable of dynamically selecting between different reactive components (jX) to streamline the optimisation process.

While various microwave switch (MS) technologies are commercially available, they often fail to meet the stringent integration requirements of an OLMBA, particularly in terms of frequency range, power handling, and technology compatibility. This challenge becomes even more pronounced when conducting extensive iterative evaluations of jX, as integrating a module-level MS with a monolithic microwave integrated circuits (MMIC) level OLMBA introduces additional technological mismatches and performance constraints.

To address this challenge, we propose the development of a switching network that adheres to stringent design specifications, including high-frequency operation, robust power handling, and seamless compatibility with GaN on SiC technology. This network is designed to precisely control the propagation of the CSP, directing it towards a specific jX component to enable dynamic impedance tuning. By ensuring a controlled RF reflection back into the OLMBA module with minimal insertion loss, the switching network optimises the RF signal at the output by preserving signal integrity through a phase-coherent reflection of the CSP. Given its ability to electronically reconfigure the presented impedance, we designate this network as a "tunable reflective termination."

Given the prolonged fabrication lead time (approximately 10 months) for each batch of

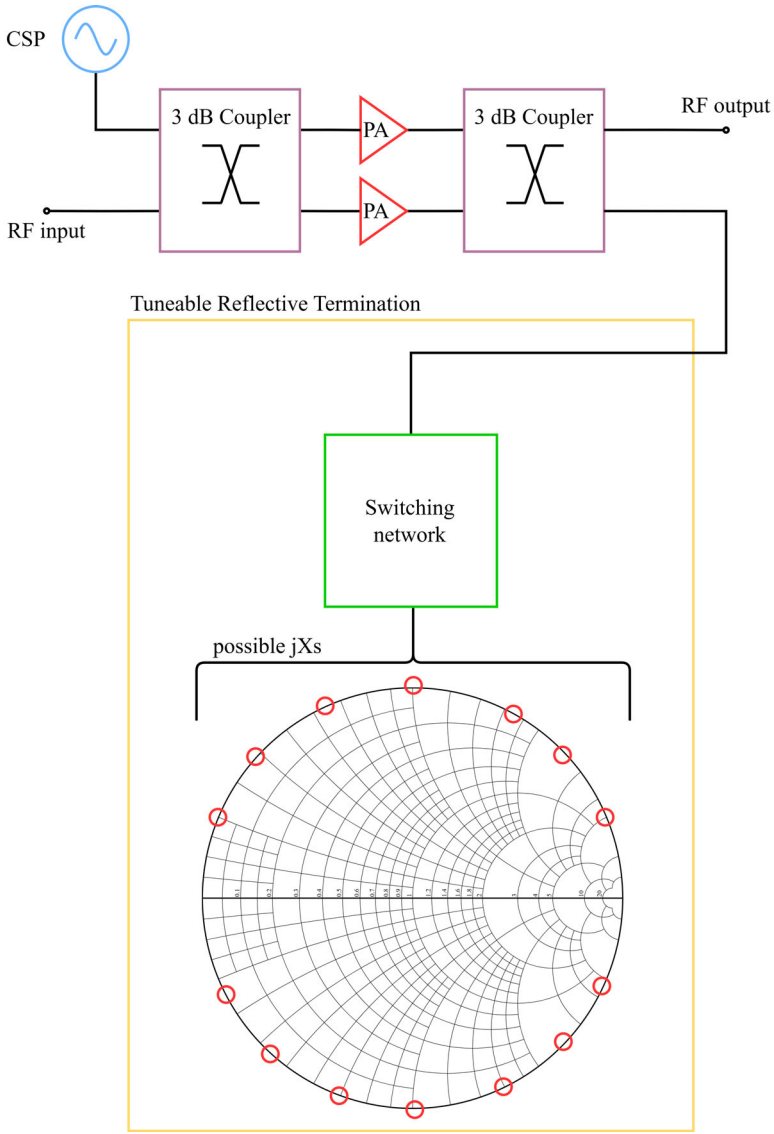

Figure 1.2: A tunable reflective termination integrated into an OLMBA via a switching network, enabling the introduction of various jX components across the Smith chart through LP implementation.

submitted designs—exceeding the two-year timeframe allocated for this work—a pragmatic decision was made to implement a switching network with two output ports as a robust and reliable design submission. However, to comprehensively characterise all possible jX scenarios, the switch underwent extensive large-signal evaluation, with a particular emphasis on LP measurements. This approach ensures a thorough analysis of the switch's behaviour when subjected to a wide range of jX values, providing critical insight into its operational performance.

Moreover, this characterisation will facilitate the development of an accurate behavioural model that captures the switch's response across a wide range of jX values, spanning

the entire Smith chart while sweeping the power to 1dB compression. The resulting behavioural model will then be integrated into CAD tools such as ADS from Keysight, allowing for a complete and precise design workflow for an OLMBA with practical and highly accurate jX representations.

Therefore, we take great pride in presenting this work as a practical development of a tunable reflective termination component, alongside the establishment of a large-signal behavioural jX model. This advancement aims to optimise OLMBA architectures for future high-frequency applications, contributing to the ongoing research efforts within the Centre for High Frequency Engineering (CHFE) group at Cardiff University.

1.2 CHAPTERS' OVERVIEW

This work is structured into eight chapters, including the introduction and conclusion, as outlined below.

Chapter 1 provides an introduction, outlining the motivation behind this research and summarising the content of the subsequent chapters.

Chapter 2 serves as the first literature review, emphasising the critical role of MS technology and comparing available switching technologies to identify the most suitable candidates.

Chapter 3 forms the second literature chapter, initially covering fundamental aspects of LP techniques. It later delves into the background of large-signal behavioural modelling, with a particular focus on the Cardiff behavioural model.

Chapter 4 published at [7], presents the first original research contribution, investigating HEMT-structured MS technology at 3 GHz as a switching cell candidate. This includes LP characterisation and the development of the first Cardiff behavioural model ever developed on MS.

Chapter 5 published at [8], extends the study to mm-wave frequencies, incorporating LP measurements with power sweeps. An advanced Cardiff model is developed, incorporating power-dependent parameters and interpolation features to enhance its predictive capabilities.

Chapter 6 published at [9], presents the design, fabrication, and characterisation of a high-power Ka-band SPDT, engineered to handle up to 3 W while maintaining low insertion loss and high isolation. Although primarily designed to facilitate tunable reflective

termination operation, its good performance also makes it a viable candidate for TxRx applications.

Chapter 7 published at [10], presents the development of a tunable reflective termination model for CAD software. The designed SPDT in chapter 6 underwent LP measurements in a non-50 Ω system to simulate various jX conditions. The extracted data is employed to develop a behavioural model, which is further optimised to enable model generation with an extremely reduced dataset.

Chapter 8 concludes this research work and its findings and highlights possible future works and gaps for further investigations.

BIBLIOGRAPHY

[1] W. Doherty, "A new high efficiency power amplifier for modulated waves," *Proceedings of the Institute of Radio Engineers*, vol. 24, no. 9, pp. 1163–1182, 1936.

[2] S. C. Cripps *et al.*, *RF power amplifiers for wireless communications*, vol. 250. Artech house Norwood, MA, 2006.

[3] K. Chen and D. Peroulis, "Design of adaptive highly efficient gan power amplifier for octave-bandwidth application and dynamic load modulation," *IEEE Transactions on Microwave Theory and Techniques*, vol. 60, no. 6, pp. 1829–1839, 2012.

[4] D. J. Shepphard, J. Powell, and S. C. Cripps, "An efficient broadband reconfigurable power amplifier using active load modulation," *IEEE Microwave and Wireless Components Letters*, vol. 26, no. 6, pp. 443–445, 2016.

[5] D. J. Collins, R. Quaglia, J. R. Powell, and S. C. Cripps, "The orthogonal lmba: A novel rfpa architecture with broadband reconfigurability," *IEEE Microwave and Wireless Components Letters*, vol. 30, no. 9, pp. 888–891, 2020.

[6] R. Quaglia, J. R. Powell, K. A. Chaudhry, and S. C. Cripps, "Mitigation of load mismatch effects using an orthogonal load modulated balanced amplifier," *IEEE Transactions on Microwave Theory and Techniques*, vol. 70, no. 6, pp. 3329–3341, 2022.

[7] S. U. Ghozati, A. Baddeley, and R. Quaglia, "Large-signal characterization and behavioral modeling of mm-wave gan hemt switches tailored for advanced power amplifier architectures," in *2024 IEEE Topical Conference on RF/Microwave Power Amplifiers for Radio and Wireless Applications (PAWR)*, pp. 21–23, 2024.

[8] S. U. Ghozati, R. Quaglia, E. Azad, J. Powell, P. Tasker, and S. Cripps, "Load pull-driven behavioral modelling of microwave switches for the design of tunable reflective terminations," in *2023 18th European Microwave Integrated Circuits Conference (EuMIC)*, pp. 1–4, 2023.

[9] S. U. Ghozati and R. Quaglia, "Ka-band single-pole double-throw switch in gan mmic technology," *International Journal of Microwave and Wireless Technologies*, p. 1–11, 2025.

[10] S. U. Ghozati, E. Mehrabi Azad, K. Chaudhry, R. Quaglia, and P. J. Tasker, "Cardiff behavioral model of a ka-band spdt switch trained on structured minimization of load-pull characterization data," in *2025 International Workshop on Integrated Nonlinear Microwave and Millimetre-Wave Circuits (INMMIC)*, pp. 1–4, 2025. In press.

CHAPTER 2

MICROWAVE SWITCH

The ultimate objective of this research is to design a tunable reflective termination intended as an enabling component for the OLMBA architecture. Achieving this requires a thorough understanding of MS-type, their network configurations (including switching device and associated passive network), and the potential active devices serving as switching cells. This chapter establishes the groundwork for the subsequent chapters by exploring the critical switching components and technologies, underlying principles, and various architectures and reviewing the evolution of these technologies. Doing so provides a comprehensive framework for the discussions and analyses presented in later sections.

Given the wide variety of components and technologies available, addressing them all would exceed the scope of this work and diverge from its primary focus. Consequently, the study is centred on solid-state field effect transistor (FET)-based devices, which align more closely with the objectives and applications of this research.

Later in this chapter, various stand-alone configurations, such as series, shunt, as well as compound networks—are discussed in terms of their switching performance, insertion loss, and isolation parameters.

2.1 INTRODUCTION

MSs are key elements to almost all communication systems. Microwave switches are designed to control and reconfigure systems by introducing variable impedances to perform signal propagation/blockage into/from a specific path. They are typically used to connect or disconnect various components in a microwave circuit, such as antennas, amplifiers, filters, mixers, and detectors, thereby facilitating signal routing and control. MSs are used in various applications such as space-based communication systems, where reconfigurability and adaptability are essential for optimal performance, support for multiple frequency bands, and changing requirements [1, 2], adaptive power amplifiers employ switchable matching networks to enhance efficiency across different frequency bands [3], RF variable attenuators and switch-type phase shifters (STPS) utilise microwave switches, enabling precise control over signal attenuation and phase manipulation [4–8], and to synthesise variable impedances (voltage/current dependent RF resistors, or inside automatic calibration kits) [9]. RF switches are also utilised in automated measurement systems to govern signal paths, facilitating efficient testing of one device under test (DUT) via multiple measurement systems, multiple DUT via multiple measurement systems, and multiple DUT via one measurement system using switch matrices [10]. Furthermore, microwave switches serve as a protective block by disconnecting subsystems to prevent excessive stress and ensure safety.

In the early days of RF technology, electromechanical switches were the primary means of controlling RF signals. These types of switches can be characterised based on the number of circuits they can connect, known as "poles," and the number of distinct positions or "throws" they can assume. As illustrated in Figure 2.1, a switch with a single pole single throw (SPST) configuration is a straightforward device that either establishes or interrupts a single circuit. On the other hand, a SPDT refers to a configuration where one input signal directs into two different outputs. The double pole double throw (DPDT) switch is a slightly more complex ON and OFF switch that simultaneously controls the connection of two inputs and outputs. Considering current technological advancements and specific

application requirements, these architectures can now be expanded to include multiple outputs/throws (MT).

The electromechanical switches can be used over wide frequency ranges, offering high power handling capability and excellent isolation with a low loss and minimum cross-talk between channels. However, they have slower switching speeds and limited reliability due to the mechanical components and electromagnetic interference caused by contact sparking. The push button switch, toggle switch, rotary switch, rocker switch, slider switch, and dual in-line package (DIP) switch are among the most encountered electromechanical switches, which are commonly employed in various applications, including telecommunications, radar systems, test and measurement equipment, and satellite communication systems.

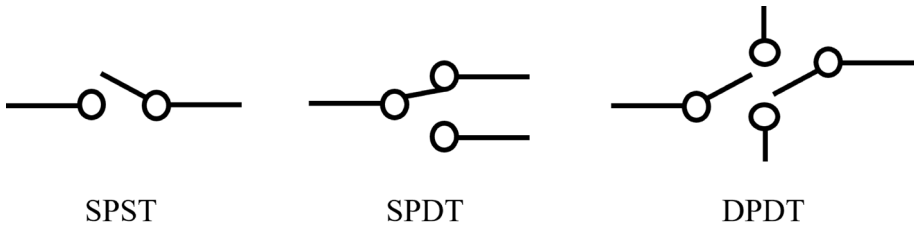

Figure 2.1: Different types of microwave switch in terms of connectivity.

The outburst of electrically controlled switches, initiated with the advent of solid-state technology, brought significant advancements in microwave switches. The introduction of positive-intrinsic-negative (PIN) diode switches revolutionised the field of microwave switches by far. Emerging compound semiconductor materials such as GaN and SiC have led to the development of high-performance FET type switches capable of handling increased power levels, better insertion loss and isolation, achieving higher efficiency, and ensuring enhanced reliability while enabling miniaturisation requirements for MMIC. The robustness of operating frequency based on an improved R_{on} in such devices can be demonstrated by the so-known artificial cut-off frequency (F_c):

$$F_c = \frac{1}{2\pi R_{on} C_{off}} \tag{2.1}$$

Where R_{on}, effectively correlates with the insertion loss in the on-state, and C_{off} characterises the isolation in the off-state [11].

Notably, RF microelectromechanical systems (MEMS) have emerged as one of the most recent and well-established technologies in the microwave switch industry, particularly in high-volume commercial markets. The term microsystem technology generally represents specific micromachined components (e.g. static micromachined, self-assembled and vibrational), microelectromechanical systems (e.g. actuated using electrostatic, piezoelectric, electromagnetic or electrothermal mechanisms) and microfluidic technologies. It is stated by [10] that, by far, the most important true RF MEMS component is the switch. MEMS switches can be used to implement high-performance digitally controlled components, reconfigurable circuits and subsystems. There are two generic types of the RF MEMS switches: I) ohmic contact (metal-air-metal (MAM)), and II) capacitive membrane (metal-insulator-metal (MIM)). The ohmic type is known to have extremely high performance due to its inherent low ON-state insertion loss and off-state isolation. As expected, a trade-off between a low on-state insertion loss and compromising the off-state isolation occurs by increasing the electrode surface area in the capacitive membrane switch.

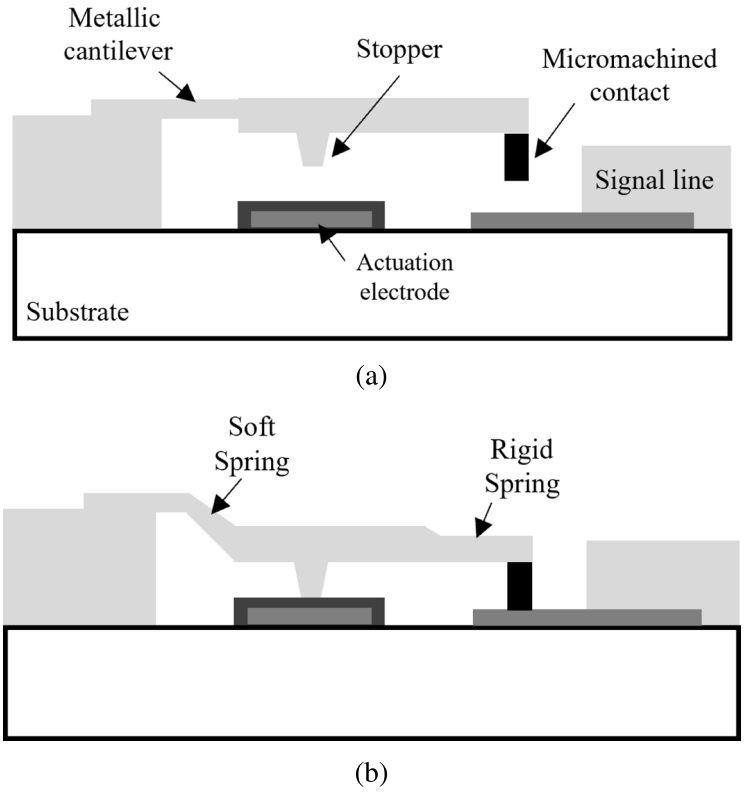

Figure 2.2: An illustration of a MEMS switch; in idle state (a), in the actuated state (b) [11].

2.2 SOLID STATE MICROWAVE SWITCHES

Moving from lower frequency applications with bigger sizes of modules with more lumped elements towards mm-wave applications with higher operating frequencies indicated a fast transition requirement from electromechanical to solid-state microwave switches. Although compared to electromechanical switches, the solid-state switches (e.g., varactors or PIN diodes) previously were suffering from higher intrinsic R_{on}, more harmonic distortion, higher insertion loss, more non-linearity and lower power handling capabilities, but still they had become the centre of attraction due to their compatibility with MMIC designs [10].

The unique properties of GaN, a III-nitride compound, make it highly advantageous for FET-based microwave switches. These include a wide bandgap and high electric field strength, which enable higher operating voltages and temperatures; high electron mobility, which enhances operating frequencies and facilitates faster switching; and high electron saturation velocity, resulting in increased output power density. Additionally, its excellent thermal conductivity ensures efficient heat dissipation. Together, these characteristics overcome traditional limitations in FET-based microwave switches, enabling superior performance at higher frequencies with reduced insertion loss, improved isolation, enhanced power handling, greater linearity, and lower DC power consumption.

MSs can either be implemented to be reflective or absorptive, depending on their design within the circuit. In the ON state, both types of switches establish a low-impedance path to the load. However, this differs when they are in the OFF state. In an absorptive type, as the name suggests, all the signals will be absorbed through a so-called terminating resistance (Z_0). In a reflective type, the signal will be reflected to its source or other path, depending on the switch circuitry. Reflection happens when an open circuit comes in cascade with the signal source, or a short circuit comes in shunt with the load, which causes the incident signal to be reflected back to the source. A cascade configuration without additional modifications is typically considered a standard reflective switch in practical applications. However, the desired absorptive and reflective behaviour functionalities can

be achieved using a shunt configuration, as illustrated in Figure 2.3.

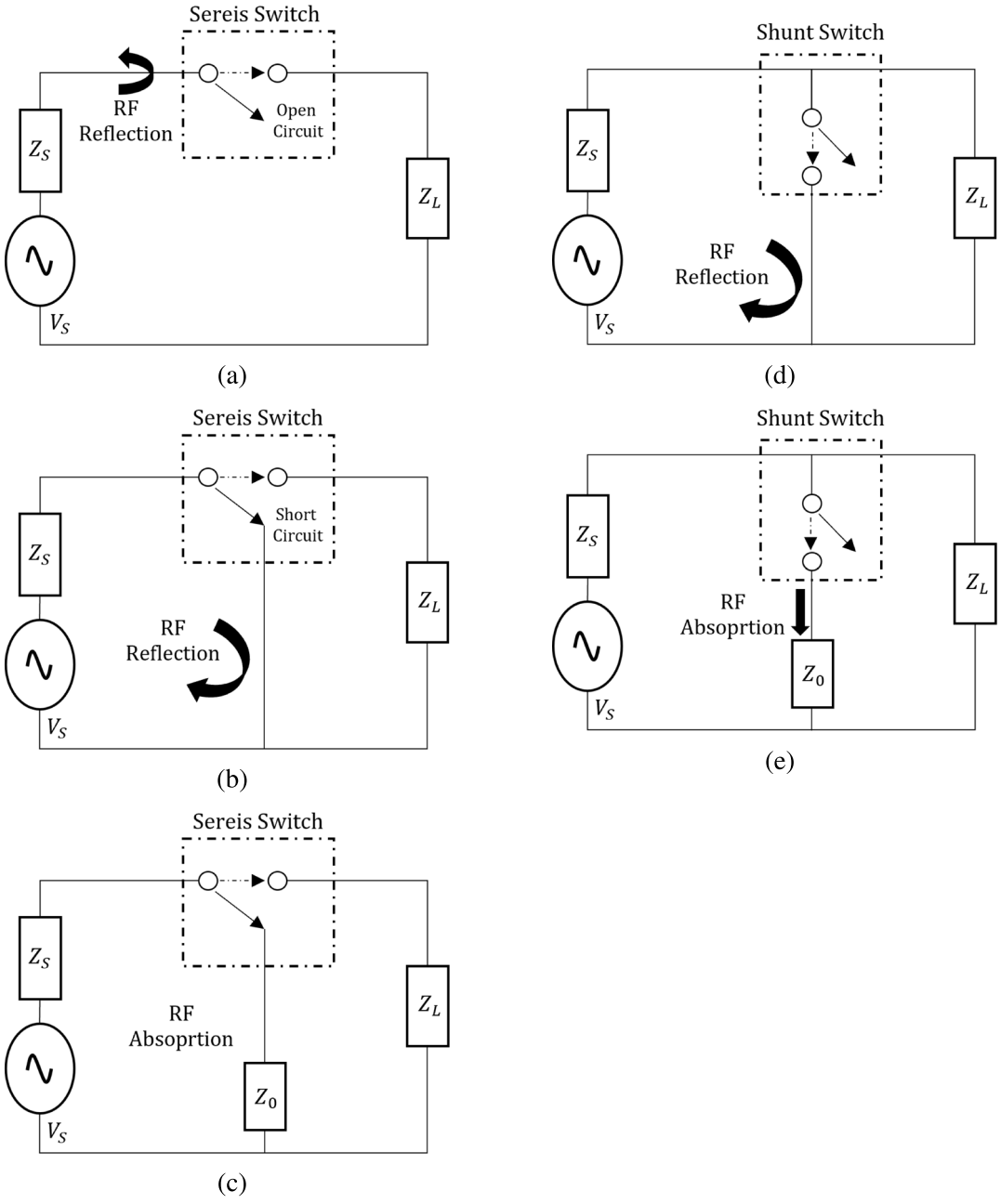

Figure 2.3: MS topologies; series reflective through cascade configuration (a), series reflective through a short path (b), series absorptive through the load (Z_0) (c), shunt reflective through a short path (d), shunt absorptive through terminating resistance (Z_0) (e).

2.3 FET-BASED MICROWAVE SWITCHES

FETs are also known as variable resistors at zero drain voltage where no amplification occurs, offer advantageous switching characteristics, including high switching speed, low

power consumption, and wide operating bandwidth, making them an attractive alternative to PIN diodes for both high- and low-frequency switching applications. Considering the high DC current requirement of the PIN diodes in their ON state and their non-linear behaviour at lower microwave frequencies opened the line of investigations on FET-based devices as MS switches. In addition, FET switches have a high capacity for signal routing with minimal signal degradation due to their low insertion loss and high isolation.

The efficiency and performance of a MS in its ON state are evaluated using a parameter known as insertion loss (IL). Insertion loss measures the ratio of signal strength between the input port, where the signal is injected, and the output port, where the signal is extracted. It is expressed in dB and is a crucial metric for assessing the switch's effectiveness in transmitting signals. Similarly, in the OFF condition of a switch, despite a shut channel, some amount of the injected signal will be managed to pass through due to various reasons (e.g. the size of the depletion region and amplitude of the injected signal in case of a FET-based switch). This breakthrough of the signal in the OFF condition of the switch determines the quality of isolation in dB units.

$$20\log_{10}(|S_{21}|)\begin{cases}\text{Insertion Loss} & if\ \text{ON}\\ \\ \text{Isolation} & if\ \text{OFF}\end{cases} \tag{2.2}$$

Where S_{21} is the parameter to characterise the insertion loss and isolation of a MS in the ON and OFF conditions, respectively. The source and load impedances are assumed to be Z_0.

A depletion mode or *n*-channel transistor is a FET type that operates with the channel already formed in its semiconductor material even when no voltage is applied to the gate terminal. It is created by doping the channel region with impurities of the opposite type compared to the source and drain regions. For example, if the source and drain are heavily doped with *n*-type impurities (extra electrons), the channel region may be lightly doped with *p*-type impurities (extra holes). Applying a negative voltage to the gate terminal of a depletion-mode transistor causes the depletion region to expand further into the channel,

narrowing the available conducting path for the current flow (increasing the resistance between the source and drain). Hence, the depletion mode FETs are more common types implemented as variable resistors for switching applications, as they show very low and very high R_{ds} in the absence and presence of gate voltage, respectively.

Ideally, the gate isolation in the channel prevents current from flowing through the gate terminal; therefore, there is no DC power dissipation, which enables an efficient broadband switch design. The gate isolation can be significantly enhanced either by incorporating a built-in big resistor or by adding an external bypass capacitor.

Moreover, FET based switches circuitry is compatible with MMIC-based microwave systems requirements, which makes them more convenient compared to PIN diodes for low-power and high-frequency applications. Among all types of FETs, metal semiconductor field effect transistors (MESFETs) and HEMTs are more attractive due to their high operating temperature inherited from high breakdown fields and high switching operation at higher frequencies inherited from two-dimensional electron gas (2DEG) channel.

In 1980, Takashi Mimura published a pioneering study on a new form of FET structured, so-called HEMT devices [12], introducing the concept of the 2DEG channel. In an HEMT, the separated electrons from their associated donor doping atoms reduce ionised impurity scatter. The term "2DEG" signifies the separation and confinement of electrons within specific epitaxial layers (epilayers), restricting their movement to a thin plane sheet (2DEG channel) due to quantum confinement. The first generation of HEMTs utilised AlGaAs/GaAs or InAlAs/InGaAs. This revolutionary technology in HEMTs, specifically involving GaN, became commercially available in 2004 when Eudyna Device Inc. in Japan introduced GaN HEMTs as depletion-mode transistors tailored for radio frequency applications.

This work utilises WIN Semiconductors GaN-on-SiC NP15 and NP12 technologies, which are designed for high-frequency and high-power applications. These technologies feature gate lengths of 150 nm and 120 nm, respectively. A more detailed discussion of these technologies will be provided in subsequent chapters.

2.3.1 Signal Models of FET-based Devices

The inherent non-linearity of high-frequency components often complicates the direct extraction of device performance metrics from their high-frequency response. Nevertheless, by segmenting the operational range into sufficiently narrow intervals, the non-linear network can be effectively linearised within each segment. This linear approximation facilitates the characterisation of device properties over these intervals, enabling the construction of an equivalent lumped-element circuit that accurately models the device's behaviour across a wide frequency spectrum. This approach, known as small-signal modelling, serves as a powerful tool for gaining deeper insights into device performance. Figure 2.4 depicts the equivalent circuit representation of a conventional HEMT-structured device configured in amplification mode.

While it is widely acknowledged that the parasitics depicted in Figure 2.4 possess a significant capability to predict device performance in its transistor mode, where

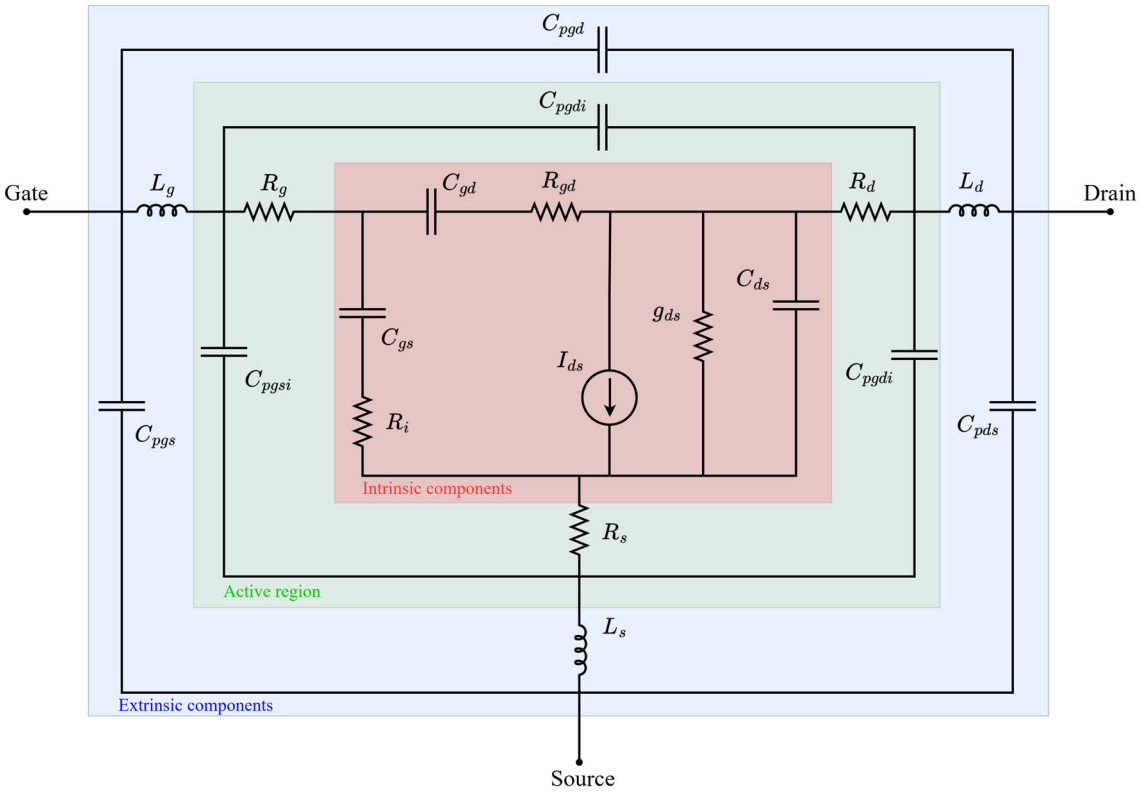

Figure 2.4: Equivalent circuit of a GaN HEMT-structured device in transistor mode based on [13, 14].

amplifications accrue, the network can be simplified in switching mode under zero drain-bias conditions. This simplification is illustrated in Figure 2.5a for the on-state (low impedance) and in Figure 2.5b for the off-state (high impedance). The accuracy of this model is validated in chapter 6 through a comparative analysis between measured data and the response of the proposed equivalent electrical circuit model.

By assuming the de-embedded pad capacitances, the on-states, Z_{TL} and off-state, Z_{TH} for both conditions can be expressed as:

$$Z_{TL} = R_{ds} + j2\pi f L_{ch} = R_{ds} + jX_L \tag{2.3}$$

$$Z_{TH} = \frac{1}{j2\pi f C_{ds}} + j2\pi f L_{ch} = -jX_C + jX_L \tag{2.4}$$

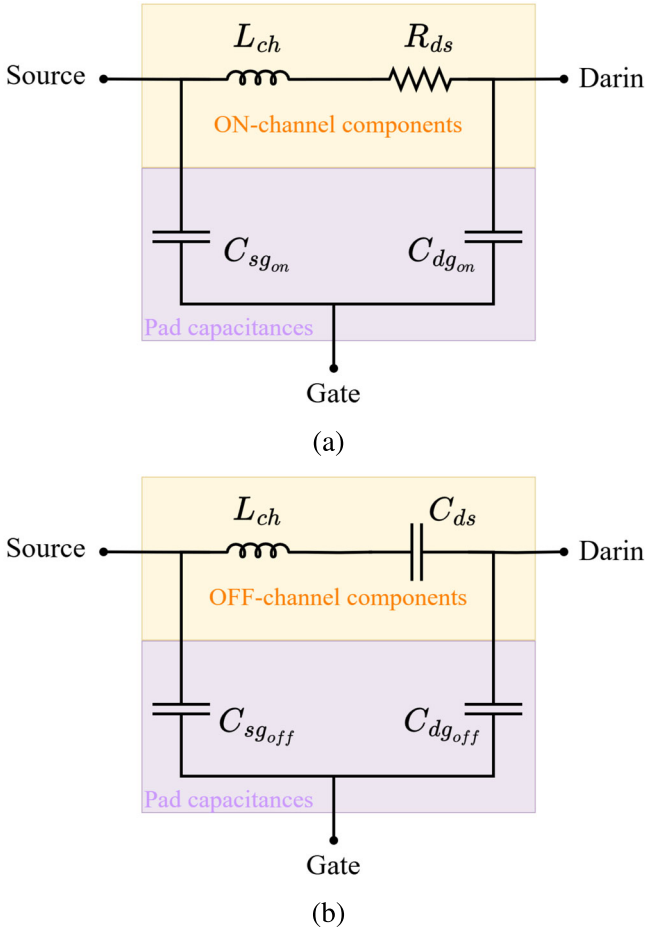

Figure 2.5: Equivalent circuit of a GaN HEMT-structured device in switching mode with zero drain voltage; ON condition (a), OFF condition (b).

2.3.2 SERIES CONFIGURATION ANALYSIS

Previously, it was mentioned that MS switches can be integrated into various topologies within the switching network. This section explores their characteristics in relation to their specific configurations.

Considering the total impedance of a switch in either low or high impedances (ON or OFF) in the series configuration in a two-port network as Z_T, can be depicted as in Figure 2.6. The source and load impedances are Z_S and Z_L, respectively. For $Z_T = 0$ assumption, the Z_S would be equal to Z_L (known as matched load where the maximum power would be transferred to the load). Therefore, voltages would have relation as $V_1 = V_2 = \frac{V_0}{2}$. It is important to know the considerations below have to be true for further derivations; I) The peak values are considered for all voltage and current components, II) Zero electrical length for the lines connecting different components, III) Finite electrical length for the double lines' connection in the schematic depicted in Figure 2.6. In this context, waves directed towards port $'n'$ are denoted as a_n, and waves moving away from port $'n'$ are referred to as b_n.

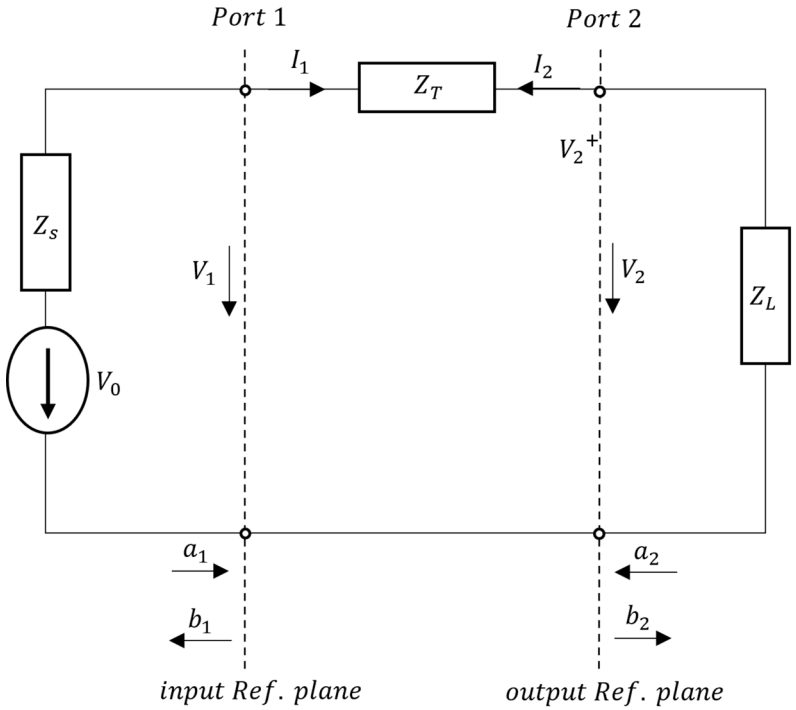

Figure 2.6: Block diagram of a stand-alone FET-based MS in series configuration.

The expression for power waves is derived by normalising the voltage waves with respect to an arbitrary reference impedance, Z_0. It is noteworthy that, conventionally, the characteristic impedance is often considered to be $50\,\Omega$ in many scenarios.

$$a_1 = \frac{V_0}{2\sqrt{Z_0}} = \frac{\text{Incident voltage at input port}}{\sqrt{Z_0}} = \frac{{V_1}^{\text{incident}}}{\sqrt{Z_0}} \tag{2.5}$$

$$b_1 = \frac{\text{Incident voltage at input port}}{\sqrt{Z_0}} = \frac{{V_1}^{\text{reflected}}}{\sqrt{Z_0}} \tag{2.6}$$

Expanding on the definitions above, the power wave can also be expressed as $a_1 = {I_1}^{\text{incident}} * \sqrt{Z_0}$, where I^{incident} denotes the incident current wave. The generalised definition of power waves (a_i and b_i) can be articulated as follows.

$$a_i = \frac{V_i + I_i Z_0}{2\sqrt{Z_0}} \tag{2.7}$$

$$b_i = \frac{V_i - I_i Z_0}{2\sqrt{Z_0}} \tag{2.8}$$

The determination of V_i and I_i can be accomplished by solving the two aforementioned equations.

$$V_i = 2\sqrt{Z_0}\, b_i + I_i Z_0 \tag{2.9}$$

$$a_i = \frac{2\sqrt{Z_0}\, b_i + I_i Z_0 + I_i Z_0}{2\sqrt{Z_0}} = \frac{2\sqrt{Z_0}\, b_i + 2 I_i Z_0}{2\sqrt{Z_0}} = \frac{\sqrt{Z_0}\, b_i + I_i Z_0}{\sqrt{Z_0}} = b_i + \frac{I_i Z_0}{\sqrt{Z_0}} \tag{2.10}$$

$$I_i Z_0 = \sqrt{Z_0}\,(a_i - b_i) \tag{2.11}$$

$$I_i = \frac{1}{\sqrt{Z_0}}\,(a_i - b_i) \tag{2.12}$$

Similarly, $V_i = \sqrt{Z_0}(a_i + b_i)$, where $V_i = {V_i}^{\text{incident}} + {V_i}^{\text{reflected}}$.

In more detailed analysis, b_i components are dependent on a_i components through a ratio known as reflection coefficients (or scattering parameters), and can be expressed as.

$$b_i = S\, a_i \tag{2.13}$$

$$b_1 = S_{11}a_1 + S_{12}a_2 \tag{2.14}$$

$$b_2 = S_{21}a_1 + S_{22}a_2 \tag{2.15}$$

The physical interpretation of S_{11} characterises when the output of the network is terminated by a matched load ($a_2 = 0$). S_{12} represents how much of a_2 is transmitted to port 1, S_{21} denotes how much of a_1 is transmitted to port 1, and S_{22} indicates how much of a_2 is reflected back at port 2.

With assumptions of $Z_S = Z_L = Z_0$, the scattering parameters can be determined by solving circuit theories and substituting the equations for voltage and current waves into the power wave expressions, yielding values based on their corresponding network impedances as follows;

$$a_1 = \frac{V_1 + I_1 Z_0}{2\sqrt{Z_0}} \quad , \quad b_1 = \frac{V_1 - I_1 Z_0}{2\sqrt{Z_0}} \quad , \quad I_1 = \frac{V_0}{2Z_0 + Z_T} \tag{2.16}$$

$$V_1 = I_1(Z_0 + Z_T) = V_0 \cdot \frac{(Z_0 + Z_T)}{2Z_0 + Z_T} \tag{2.17}$$

with $S_{11} = \frac{b_1}{a_1}$

$$S_{11} = \frac{V_1 - I_1 Z_0}{V_1 + I_1 Z_0} = \frac{Z_T}{2Z_0 + Z_T} \tag{2.18}$$

Similarly,

$$-I_2 = \frac{V_0}{2Z_0 + Z_T} \quad , \quad V_2 = I_2 Z_0 = V_0 \cdot \frac{Z_0}{2Z_0 + Z_T} \tag{2.19}$$

$$S_{22} = \frac{b_2}{a_2} = \frac{V_2 - I_2 Z_0}{V_2 + I_2 Z_0} = \frac{Z_T}{2Z_0 + Z_T} \tag{2.20}$$

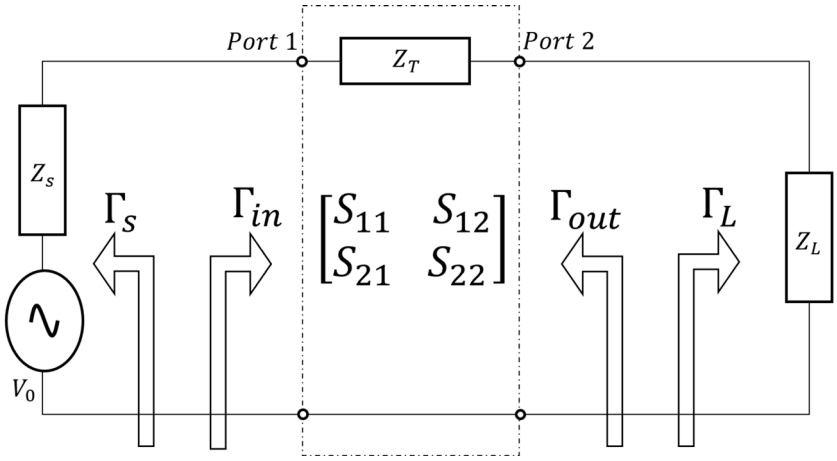

Figure 2.7: Reflection coefficients demonstration based on a stand-alone FET-based MS in series configuration.

In similar fashion S_{21} and S_{12} can be formulated as below

$$S_{21} = \frac{b_2}{a_1} = \frac{V_2 - I_2 Z_0}{V_1 + I_1 Z_0} = \frac{2Z_0}{2Z_0 + Z_T} \tag{2.21}$$

$$S_{12} = \frac{b_1}{a_2} = \frac{V_1 - I_1 Z_0}{V_2 + I_2 Z_0} = \frac{2Z_0}{2Z_0 + Z_T} \tag{2.22}$$

It is important to note due to symmetry assumptions, the components $S_{11} = S_{22}$ and $S_{21} = S_{12}$. Hence, the matrix of scattering parameters (S-parameters) of a series switch in a 2-port network can be written as below

$$\begin{bmatrix} S_{11} & S_{12} \\ S_{21} & S_{22} \end{bmatrix} = \begin{bmatrix} \frac{Z_T}{Z_T + 2Z_0} & \frac{2Z_0}{Z_T + 2Z_0} \\ \frac{2Z_0}{Z_T + 2Z_0} & \frac{Z_T}{Z_T + 2Z_0} \end{bmatrix} \tag{2.23}$$

The source and load reflection coefficients (Γ_S and Γ_L, respectively) can be derived with respect to Z_0 as below.

$$\Gamma_S = \frac{Z_S - Z_0}{Z_S + Z_0} \tag{2.24}$$

$$\Gamma_L = \frac{Z_L - Z_0}{Z_L + Z_0} \tag{2.25}$$

The availability of source and load reflection coefficients, combined with S-parameters, allows for the derivation of the Γ_{IN} and Γ_{Out}.

$$\Gamma_{IN} = S_{11} + \frac{\Gamma_L S_{12} S_{21}}{1 - \Gamma_L S_{22}} = \frac{Z_T + Z_L - Z_0}{Z_T + Z_L + Z_0} \tag{2.26}$$

$$\Gamma_{Out} = S_{22} + \frac{\Gamma_S S_{12} S_{21}}{1 - \Gamma_S S_{11}} = \frac{Z_T + Z_S - Z_0}{Z_T + Z_S + Z_0} \tag{2.27}$$

The ratio of the P_{avs} to the P_L in a series configuration based on the equations above can now be written as

$$\frac{P_{avs}}{P_L} = \left[\frac{|1 - \Gamma_S \Gamma_{IN}|^2}{1 - |\Gamma_S|^2}\right]\left[\frac{1}{|S_{21}|^2}\right]\left[\frac{|1 - S_{22}\Gamma_L|^2}{1 - |\Gamma_L|^2}\right] \tag{2.28}$$

Hence, the series-connected switch's insertion loss and isolation can be computed by substituting reflection coefficients' values into the equation above. The first and final terms denote losses caused by input and output mismatches, and the middle term signifies the switch's loss when both ports are terminated to the reference impedance, Z_0.

$$\frac{1}{|S_{21}|^2} = \left[\frac{2Z_0 + Z_T}{2Z_0}\right]^2 \tag{2.29}$$

The insertion loss parameter can be evaluated by assuming an equal resistive load and source impedance, i.e., R_0 instead of Z_0.

$$Z_T = R_{ds} + j2\pi f L_{ch} = R_{ds} + jX_L \tag{2.30}$$

$$\text{IL} = \frac{1}{|S_{21}|^2} = \left[\frac{2R_0 + R_{ds} + jX_L}{2R_0}\right]^2 \tag{2.31}$$

or

$$\text{IL } (in \text{ dB}) = 10 \log_{10}\left[(1 + \frac{R_{ds}}{2R_0})^2 + (\frac{X_L}{2R_0})^2\right] \tag{2.32}$$

Similarly, the isolation parameter can be evaluated by assuming as below,

$$Z_T = 2j\pi f L_{ch} + \frac{1}{(j2\pi f C_{ds})} = jX_L - jX_C \tag{2.33}$$

$$\text{Isolation} = \frac{1}{|S_{21}|^2} = \left[\frac{2R_0 + j(X_L - X_C)}{2R_0}\right]^2 \tag{2.34}$$

or

$$\text{Isolation } (in \text{ dB}) = 10\log_{10}\left[(1 + 4\pi f L_{ch} + \frac{1}{4\pi f C_{ds} R_0})^2\right] \tag{2.35}$$

The insertion loss, given by Equation 2.31, depends on the drain-source resistance (R_{ds}), the characteristic impedance (R_0), and the inductive reactance (X_L). This metric quantifies the signal attenuation when the switch is in the ON state. On the other hand, the isolation, expressed as Equation 2.34, is influenced by the capacitive reactance (X_C) and inductive reactance (X_L), representing the switch's ability to block signals in the OFF state. These equations highlight the trade-offs between resistance and reactance in achieving optimal switch performance, as well as their inherent dependency on frequency.

2.3.3 Shunt Configuration Analysis

In RF switches, a shunt architecture produces an inverse effect on the circuit operation. Specifically, when the switch is in the OFF state, exhibiting high impedance, the circuit functions as ON. Conversely, in the ON state, where the switch has low impedance, the circuit is effectively OFF. However, the overall impedance of the switch and its corresponding equivalent circuit remains constant for both high and low-impedance states, as previously outlined. The shunt architecture of a single HEMT device is illustrated in Figure 2.8.

Network analysis and having the equivalent circuit in shunt configuration enables to define S-parameters matrix with respect to reference impedance for a two-port network.

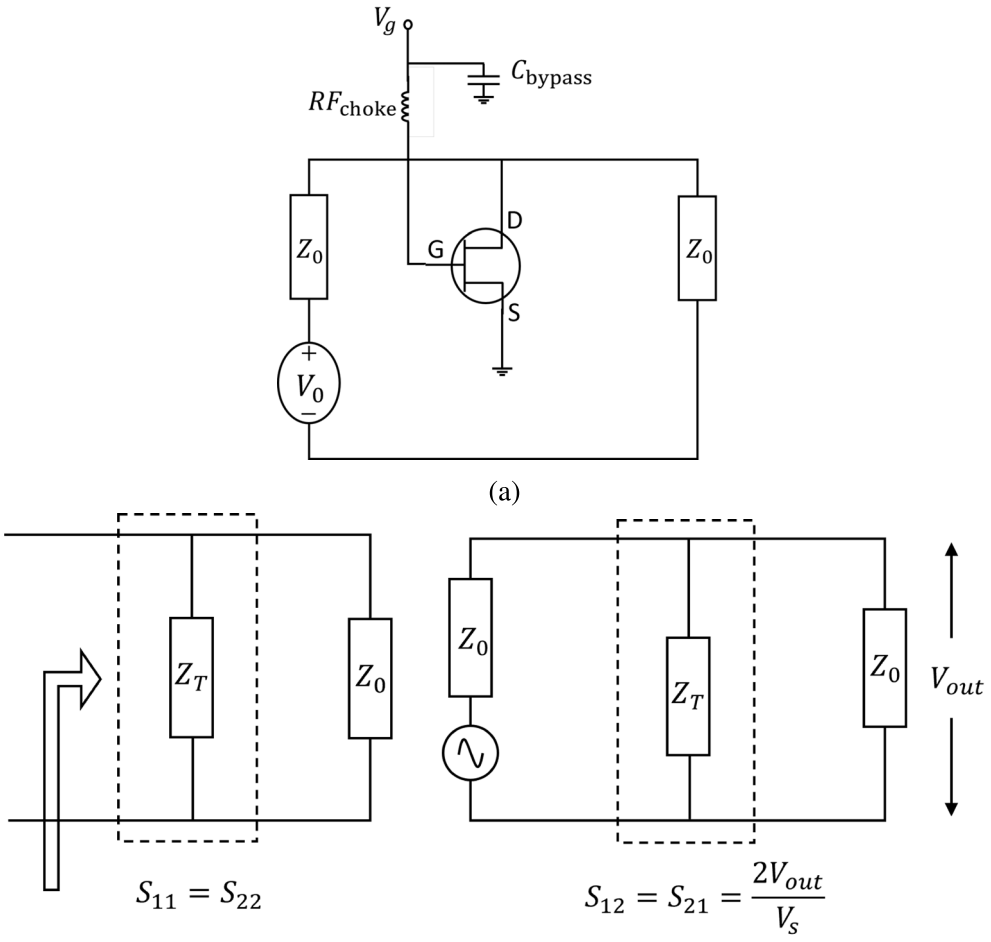

Figure 2.8: FET-based microwave switch in shunt configuration (a); network analysis of the total impedance correspond to the load to determine; the S_{11} and S_{22} (b), the S_{21} and S_{12} (c).

$$\begin{bmatrix} S_{11} & S_{12} \\ S_{21} & S_{22} \end{bmatrix} = \begin{bmatrix} \frac{Z_T||Z_0 - Z_0}{Z_T||Z_0 + Z_0} & \frac{2Z_T}{2Z_T + Z_0} \\ \frac{2Z_T}{2Z_T + Z_0} & \frac{Z_T||Z_0 - Z_0}{Z_T||Z_0 + Z_0} \end{bmatrix} = \begin{bmatrix} \frac{-Z_0}{2Z_T + Z_0} & \frac{2Z_T}{2Z_T + Z_0} \\ \frac{2Z_T}{2Z_T + Z_0} & \frac{2Z_T}{2Z_T + Z_0} \end{bmatrix}$$

The source and load reflection coefficient equations follow a series configuration. With respect to the source (Z_S) and load (Z_L) impedances, the input and output reflection

coefficients can be expressed as:

$$\Gamma_{\text{IN}} = \frac{Z_T||Z_L - Z_0}{Z_T||Z_L + Z_0} \tag{2.36}$$

$$\Gamma_{\text{Out}} = \frac{Z_T||Z_S - Z_0}{Z_T||Z_S + Z_0} \tag{2.37}$$

The ratio of the P_{avs} to the P_L in a shunt configuration follows the same formulation as given in Equation 2.28. As in series-connected, the first and last terms of Equation 2.28 represent losses due to input and output load mismatch, respectively, for the shunt-connected circuit. Assuming input and output ports both terminated to reference impedance (Z_0) at the same time, then the loss of switch can be written as

$$\frac{1}{|S_{21}|^2} = \left[\frac{2Z_T + Z_0}{2Z_T}\right]^2 = \left[1 + \frac{Z_0}{2Z_T}\right]^2 \tag{2.38}$$

The insertion loss can now be calculated combining Equation 2.4 and Equation 2.38 under the assumption of equal and purely resistive source and load impedances ($Z_0 = R_0$).

$$\text{Insertion Loss} = \left[1 + \frac{Z_0}{2Z_T}\right]^2 = \left[1 - \frac{R_0}{j\,2(X_C + X_L)}\right]^2 \tag{2.39}$$

Similarly, the OFF state isolation can be calculated employing Equation 2.3 and Equation 2.38 under the same assumption of $Z_0 = R_0$.

$$\text{Isolation} = \left[1 + \frac{Z_0}{2Z_T}\right]^2 = \left[1 + \frac{R_0}{2(R_{ds} + jX_L)}\right]^2 \tag{2.40}$$

As depicted in Figure 2.8a, in shunt-configured microwave switches, evaluating insertion loss and isolation involves using reversed impedance states compared to the series configuration. As demonstrated in Equation 2.39 the switch must be in its high capacitive impedance state (OFF state, Z_{TH}) for insertion loss analysis, enabling the signal to propagate through the main transmission line with minimal attenuation. Similarly, to analyse the isolation in the shunt configuration switch is to effectively ground the signal path, hence, it should be biased in its low-impedance state (ON state, Z_{TL}), as in Equation 2.40.

So far, the stand-alone FET-based MSs were discussed mathematically based on their positioning relative to the output load. Figure 2.9 illustrates the evaluation of the same figure of merits (FOMs), namely insertion loss and isolation, using the process design kit (PDK) of identical devices with a gate length of 150 µm and a gate width of 100 µm in a five-gate-finger channel configuration. These devices, fabricated using GaN on SiC technology, were analysed under consistent biasing conditions but in different circuit topologies: single-device-series and single-device-shunt configurations. The results, shown in Figure 2.10a and Figure 2.10b, highlight the superior isolation performance of the series configuration and the improved insertion loss in the shunt configuration. This analysis underscores the motivation for exploring more complex networks that combine series and shunt architectures to optimise performance.

Analysing insertion loss in a series architecture requires the device to be in the ON state, characterised by a low-impedance condition (Z_{TL}=R_{ds}+X_L). Conversely, assessing the same insertion loss in a shunt configuration demands the device to be in the OFF state, representing a high-impedance condition (Z_{TH}=X_C+X_L).

To evaluate the insertion loss in the series configuration, the on-state resistance (R_{ds}), a frequency-independent figure of merit that enables low-loss signal transfer, plays a critical role, as illustrated in Figure 2.10b. In contrast, the shunt configuration is influenced by the frequency-dependent nature of the off-state capacitive reactance (X_C), expressed as X_C = 1/2 .π .f .C. At lower frequencies, the high impedance in the off-state enables superior

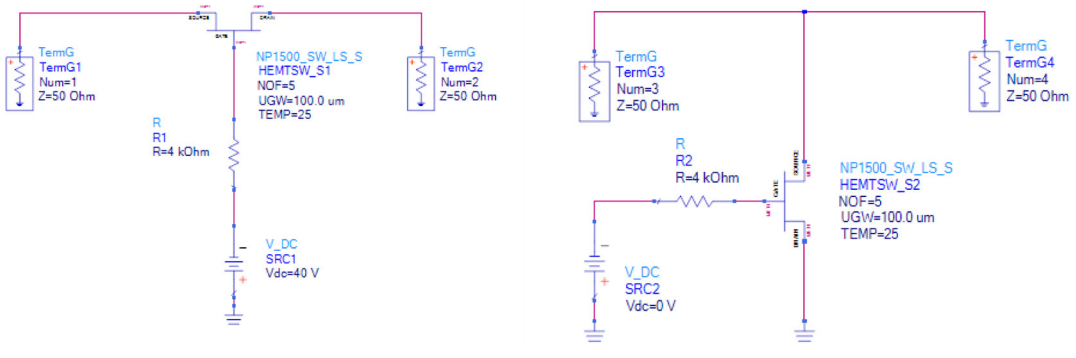

(a) (b)

Figure 2.9: Circuit diagrams of stand-alone MS implementations using WIN Semiconductors PDK; series configuration (a), shunt configuration (b).

isolation, making the shunt configuration advantageous for achieving lower insertion loss. However, as the frequency increases, the capacitive reactance decreases, leading to a reduction in the desired high off-state impedance. This results in increased losses, causing the device's performance to degrade as the frequency rises, directly impacting its optimal operation at higher frequencies.

Conversely, evaluating the FOM for isolation necessitates the device to operate in a high-impedance state in the series configuration, whereas in the shunt configuration, an on-state low-impedance is required. At lower frequencies, the frequency-dependent capacitive reactance (X_C) in the off-state (high impedance) ensures superior isolation in the series arrangement. At lower frequencies, the substantial degradation in the shunt arrangement can also be attributed to the significant role of grounding, which is now in cascade with the shunt switch.

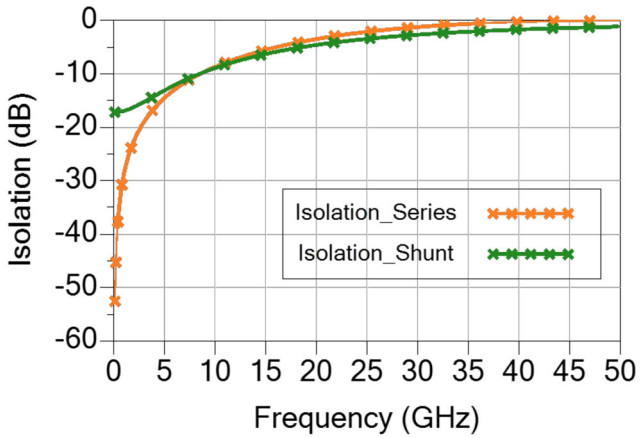

(a)

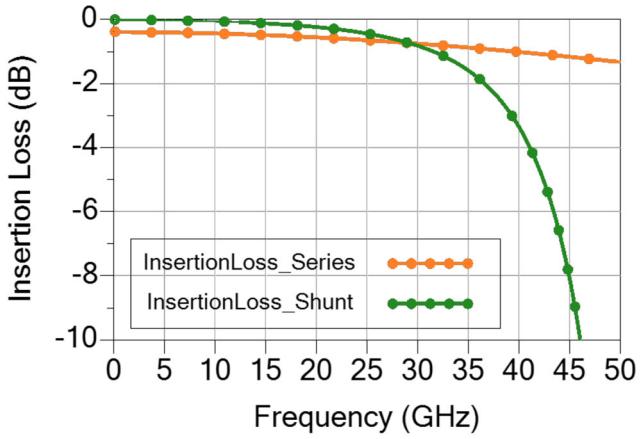

(b)

Figure 2.10: Simulated performance comparison of the 5F100 device in stand-alone topology using WIN Semiconductors PDK; isolation (a), insertion loss (b).

2.3.4 Compound Networks

In RF switch applications, a compound arrangement of switches is often used for optimising performance, enhanced functionality, and versatility. The compound configuration leverages from series FETs in achieving better isolation and shunt FETs in achieving superior insertion loss, as it is evident in Figure2.10a and 2.10b, respectively. The combination of series and shunt FETs ensures effective switching between the ON and OFF states, offering a balanced trade-off between insertion loss and isolation.

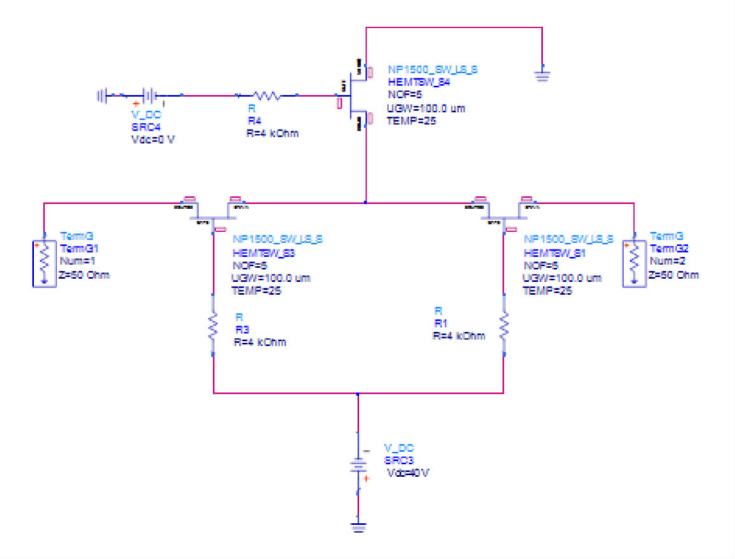

(a)

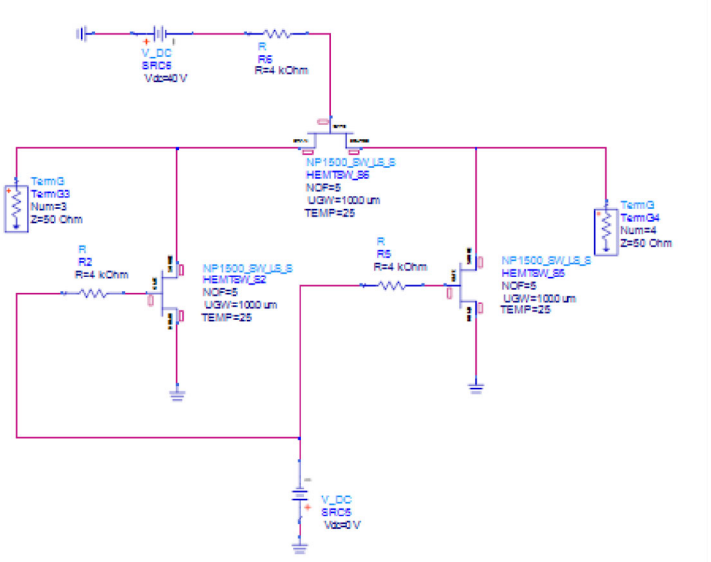

(b)

Figure 2.11: Compound networks schematics; T-type network (a) and π-type network (b).

To enable the operation of series and shunt FETs in their respective switch states, opposite or complementary conduction states are required, which in turn necessitate opposite or complementary gate biases. The two most common compound network configurations; T-type and π-type, are illustrated in Figure,2.11.

Similarly, the insertion loss and isolation of the two presented compound networks are analysed through CAD simulations using the same PDK implementing the identical devices and same biasing conditions. Figure 2.12a expresses more enhanced isolation at higher frequencies for both T-type and π-type compared to stand-alone performance depicted in Figure 2.10. In assessing the insertion loss, both compound networks exhibit sufficiently flat responses up to approximately mm-wave frequencies. This behaviour can be directly

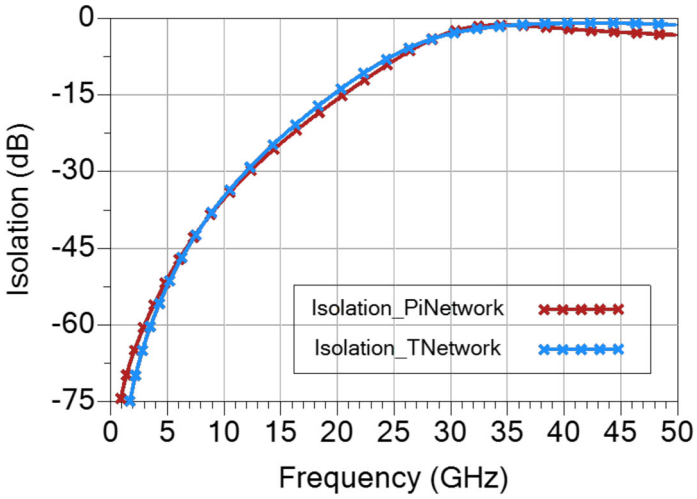

(a)

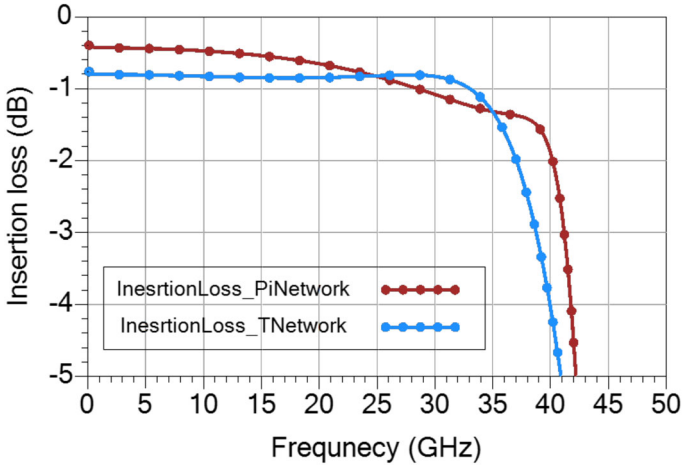

(b)

Figure 2.12: Compound networks small signal simulation results; isolation (a), insertion loss (b)

associated with the technology-dependent cut-off frequency product (F_c). However, the instability observed in the insertion loss at higher frequencies may be mitigated through the implementation of passive networks and complementary components to enhance overall performance.

It is important to note that all results depicted in Figures 2.10a, 2.10b, 2.12b, and 2.12a are obtained from basic device-level simulations. Notably, no isolation is achieved at higher frequencies, which is attributed to the OFF-state capacitances demonstrating an inherent inability to filter out mm-wave frequencies. This limitation must be addressed and compensated for in the final design. Chapter 6 will explore the root causes of this performance degradation and present various techniques to mitigate it in the design of mm-wave switching networks.

2.4 Millimetre Wave Switch Applications

In the domain of RF/microwave and mm-wave applications, achieving reconfigurability and multiple-band functionality is of paramount importance. This flexibility necessitates alterations in signal path, signal level, and signal phase. The mm-wave switches play a pivotal role in meeting these requirements. For instance, a power amplifier with a tunable frequency band can be realised by employing switches to alternate between matching networks. Automated measurements become feasible by utilising switching networks to measure multiple devices or test one device with various instruments and setups. Protective circuit designs can leverage switching concepts to prevent overstress, such as disconnecting high-level transmitted power from the receiver in radar systems that use a single antenna for both transmission and reception, known as a TxRx. In a TxRx application, the antenna is connected to a transmitter in the transmit state and a receiver in the receive state. Figure 2.13a illustrates a TxRx application, and by implementing identical switches, it becomes evident that a TxRx block diagram can be implemented through a SPDT switching network, as depicted in Figure 2.13b.

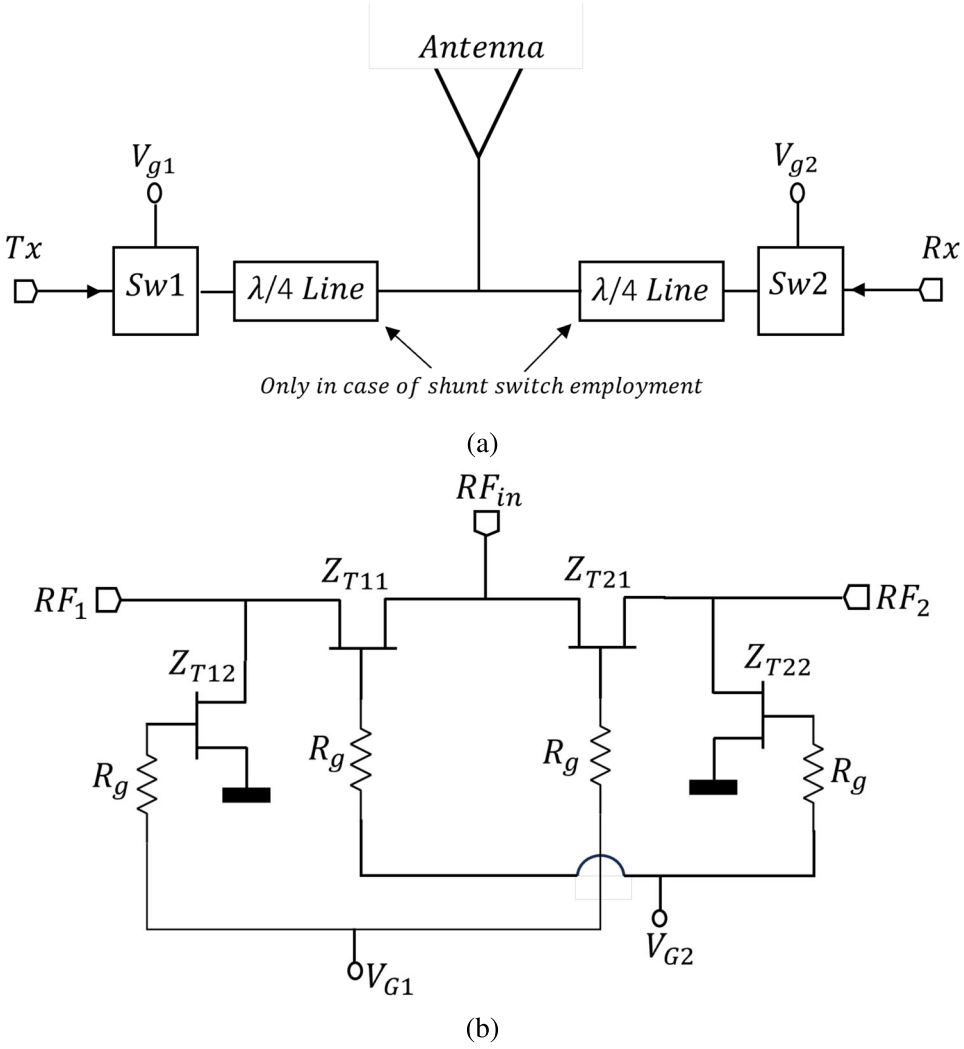

Figure 2.13: Single antenna with both transmitting and receiving functionality (TxRx) (a), a block diagram of an SPDT which represent the same functionality as in TxRx (b).

2.4.1 Single Pole Double Throw Application

SPDT is a type of RF switching topologies that has one input terminal, also referred to as the common terminal, and two other output terminals, also known as the throw terminals. The SPDT switch provides versatility in circuit design to enable the selection between two different signal paths and also to optimise either the isolation and/or insertion loss, making it useful in scenarios where signal routing between two states is required. Its simplicity, reliability, and ease of implementation make it a popular choice in many electronic applications.

Figure 2.13b illustrates a commonly used architecture for designing an SPDT switch. This configuration combines series and shunt topologies at each port, requiring only two

complementary voltages for operation. Assuming the port named RF_{in} hosts the input signal, the signal can be directed toward either RF1 or RF2 ports. To route the signal to the active port (e.g., RF1), the series and shunt FETs should be set to low- and high-impedance states, respectively. Simultaneously, complementary voltages should be applied to the corresponding FETs at the inactive port (e.g., RF2) to ensure isolation. A sufficiently large R_g can provide isolation for the gate circuitry. Furthermore, reflective and absorptive architectures can be implemented within compound topologies. For instance, as depicted in Figure 2.13b, shunt devices can be configured to reflect the signal back to the source, forming a reflective architecture. Alternatively, terminating the signal to an impedance equal to the characteristic impedance (Z_0) creates an absorptive architecture.

The implementation of an SPDT and its optimal performance can vary significantly depending on the switching cell technology, operating frequency, and design constraints such as size limitations. Although TxRx systems represent a typical application for SPDT switches, this work focuses on developing an SPDT specifically tailored for the development of the tunable reflective termination application mm-wave frequencies, as detailed in subsequent chapters.

BIBLIOGRAPHY

[1] A. Barigelli, F. Diaferia, P. Panfili, M. Scipioni, F. Vitulli, A. Biondi, D. Resca, F. Scappaviva, G. Nicolai, and D. D. Gregorio, "Scalable ka band switch matrix in compact ltcc package for satellite communication application," *2017 12th European Microwave Integrated Circuits Conference (EuMIC)*, pp. 333–336, 2017.

[2] G. L. Lan, D. Dunn, J. Chen, C. keng Pao, and D. Wang, "A high performance v-band monolithic fet transmit-receive switch," *IEEE 1988 Microwave and Millimeter-Wave Monolithic Circuits Symposium. Digest of Papers.*, pp. 99–101, 1988.

[3] M. Lee and C. Park, "A triple-band cmos power amplifier using multi-band and switchable matching network for wireless mobile," *IEEE Transactions on Microwave Theory and Techniques*, vol. 67, no. 10, pp. 4220–4231, 2019.

[4] Y. Tajima, T. Tsukii, R. Mozzi, E. Tong, L. Hanes, and B. Wrona, "Gaas monolithic wideband (2-18 ghz) variable attenuators," in *1982 IEEE MTT-S International Microwave Symposium Digest*, pp. 479–481, 1982.

[5] S. Daoud and P. Shastry, "A novel wideband mmic voltage controlled attenuator with a bandpass filter topology," *IEEE Transactions on Microwave Theory and Techniques*, vol. 54, no. 6, pp. 2576–2583, 2006.

[6] H. Dogan, R. G. Meyer, and A. M. Niknejad, "Analysis and design of rf cmos attenuators," *IEEE Journal of Solid-State Circuits*, vol. 43, no. 10, pp. 2269–2283, 2008.

[7] P. Gu and D. Zhao, "A ka-band cmos switched-type phase shifter with low gain error,"

in *2021 IEEE International Conference on Integrated Circuits, Technologies and Applications (ICTA)*, pp. 175–176, 2021.

[8] Y.-J. Liang, K.-C. Chiang, Y.-H. Lin, H. Alsuraisry, J.-H. Tsai, and T.-W. Huang, "A 19-ghz 5-bit switch-type phase shifter design using phase compensation techniques," in *2021 IEEE International Symposium on Radio-Frequency Integration Technology (RFIT)*, pp. 1–3, 2021.

[9] F. Drillet, J. Loraine, H. Saleh, I. Lahbib, B. Grandchamp, L. Iogna-Prat, I. Lahbib, O. Sow, A. Kumar, and G. U'Ren, "Rf small and large signal characterization of a 3d integrated gan/rf-soi spst switch," *International Journal of Microwave and Wireless Technologies*, vol. 13, no. 6, pp. 517–522, 2021.

[10] S. C. Bera, *Microwave active devices and circuits for communication*. Springer, 2019.

[11] S. Lucyszyn, *Advanced RF MEMS*. The Cambridge RF and Microwave Engineering Series, Cambridge University Press, 2010.

[12] T. Mimura, S. Hiyamizu, T. Fujii, and K. Nanbu, "A new field-effect transistor with selectively doped gaas/n-alxga1-xas heterojunctions," *Japanese Journal of Applied Physics*, vol. 19, p. L225, may 1980.

[13] R. Singh and C. Snowden, "Small-signal characterization of microwave and millimeter-wave hemt's based on a physical model," *IEEE Transactions on Microwave Theory and Techniques*, vol. 44, no. 1, pp. 114–121, 1996.

[14] J. W. Chung, *Millimeter-wave GaN high electron mobility transistors and their integration with silicon electronics*. PhD thesis, Massachusetts Institute of Technology, 2011.

CHAPTER 3

LOAD-PULL MEASUREMENT OF MICROWAVE SWITCHES AND CARDIFF BEHAVIOURAL MODEL

This chapter establishes the theoretical and literature foundation for the subsequent chapters, where practical load-pull measurements are implemented on microwave switches. Additionally, it paves the way for the development of the first Cardiff behavioural model specifically tailored for microwave switches.

In the first section, the principles and techniques of LP measurement are explored in detail. This includes an examination of the systems and methodologies employed in LP measurements, providing a foundational understanding of their application in high-frequency systems.

In the later sections of this chapter, the focus shifts to behavioural modelling, with particular emphasis on the Cardiff behavioural model developed to date. This discussion will highlight the key aspects of the model and its relevance to high-frequency device characterisation.

3.1 Load-Pull Measurement

3.1.1 Introduction

The S-parameters can describe a network stimulated with small incident signals that cause linear behaviour at a specific frequency. Therefore, using S-parameters to design non-linear applications is infeasible. Golio et al. [1] state that nearly all microwave circuits and systems exhibit some non-linear behaviour. He explains some of the methods developed to better understand the effects of nonlinearity on signals and systems. Cripps et al. [2] comprehensively discussed how the drive for greater efficiency and power in modern RF and microwave (MW) applications, like PAs across various classes, often involves non-linearities. Nonetheless, these non-linearities require more complex characterisation techniques.

The measurement of large signals involves the use of specialised instruments and various techniques. The LP measurements are a highly regarded large signal characterisation technique due to their ability to quickly and accurately characterise microwave devices. The initial implementations and applications of contemporary LP techniques can be traced back to the 1940s, where the "Rieke diagram" was employed to illustrate how the performance of microwave tubes varied as a function of the load impedance [3].

The optimal operation of RF components is achievable only when optimal conditions are established for the source and load parameters. The LP measurements play a vital role in this process, identifying optimal conditions by introducing various impedances to the port under test while sweeping other variables, such as power levels or frequencies, facilitating the fine-tuning of essential parameters, such as output power, gain, and efficiency. The extracted data is based on impedance manipulation and fitting contours within the Γ domain. Teppati et al.,[3] discuss some representative applications of LP such as: matching network design, large-signal modelling, technology process development, and reliability testing including failure identification.

Since the primary objective of this work is to develop a tunable reflective termination, LP measurements are essential—not only for characterising the switching devices but also

for providing the necessary data for model generation.

3.1.2 Load-Pull Principles

Modern microwave measurements involve using a set of parameters called *power waves* to analyse the collected data. These parameters and their advantages in characterising the power transferred between a source and a load are thoroughly explained by Pozar [4]. Equations 3.1 and 3.2 represent these power waves, denoted as the incident power wave amplitude (A) and reflected power wave amplitude (B), derived from a linear transformation of the total voltage and current in the frequency domain.

$$A = \frac{V + Z_R I}{2\sqrt{Z_R}} \tag{3.1}$$

$$B = \frac{V - Z_R^* I}{2\sqrt{Z_R}} \tag{3.2}$$

Where $Z_R = R_R + jX_R$ is referred to as *reference impedance*, which can consist of both resistive and reactive components or only the resistive component. The LP measurement captures data on the A and B components in terms of their amplitude and phase.

Figure 3.1 illustrates a single tone generic LP concept with a load tuner which controls the load impedance and the assumption that the DUT has a matched input to the source. Load tuner variations result in variations in the travelling wave components (A_2 and B_2) and, consequently, the corresponding Γ. In the single-tone test assumption, Equations 3.3 and 3.4

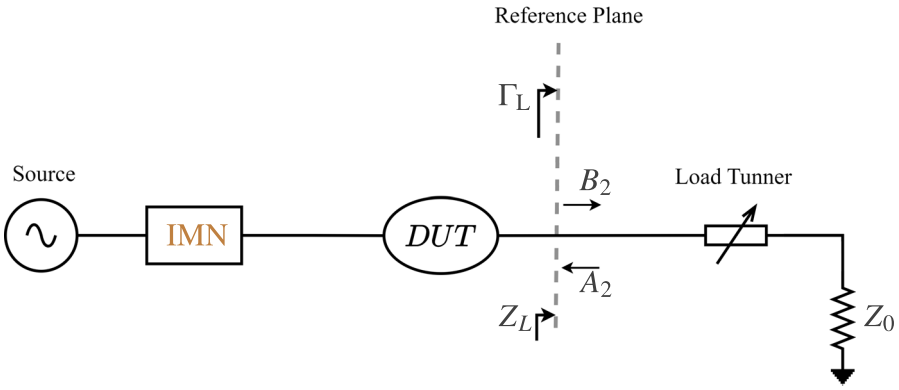

Figure 3.1: Complex load reflection coefficient (Γ_L) corresponding to the load impedance (Z_L) variations.

mathematically explain the relationships between the Z_L and travelling wave components variations and changes in the Γ_L, regardless of the pre-matched impedance condition at the network's input. Here, Z_0 represents the reference impedance of the depicted two-port network. This dynamic interaction underscores the role of load conditioning in optimising specific parameters.

$$\Gamma_L = \frac{Z_L - Z_0}{Z_L + Z_0} \tag{3.3}$$

$$\Gamma_L = \frac{A_2}{B_2} \tag{3.4}$$

Frequency domain-based LP involves varying the load impedance at the controlled F_0. Given that a DUT with large signal excitation generates uncontrolled h of the fundamental frequency, such as $2F_0$ and $3F_0$, as depicted in Figure 3.2, it underscores the generations of power waves for each harmonic and so the necessity for harmonic solutions during LP

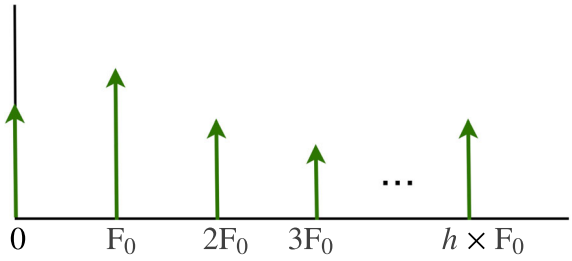

Figure 3.2: Signal representation in the frequency domain with generated harmonics of the fundamental frequency (F_0).

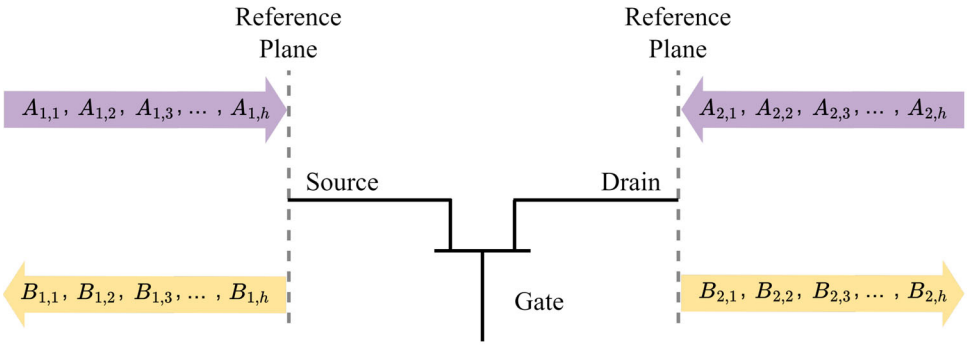

Figure 3.3: Illustration of an active device in switching configuration and corresponding travelling waves at input and output ports incorporating harmonic variables.

measurement.

Figure 3.3 illustrates the incident (A) and reflected (B) travelling waves on an active device symbol in a switching configuration. Here, the *source* serves as the input or port one, the *drain* as the output or port two, and the *gate* contact is instrumental in opening or closing the channel, providing control over the wave flow without amplification. This arrangement differs from the conventional transistor mode where *gate* and *drain* act as ports one and two, respectively, hosting incident and reflected travelling waves. Equation 3.5 presents a revised form of the previously formulated Γ_L and travelling wave components, incorporating harmonic variables. The discussion of harmonics will be further elaborated later in this chapter.

$$\Gamma_{L,h} = \frac{A_{2,h}}{B_{2,h}} \tag{3.5}$$

LP data can be utilised to monitor parameters such as (not limited) input power (P_{IN}), output power (P_{OUT}), power gain (G_P), transducer gain (G_T), power added efficiency (PAE). Figure 3.4a illustrates an example of LP data implementation on the Smith Chart, showcasing 0.3 dB power contours to identify optimum Γ corresponding to the maximum output power. The optimal load can be determined by evaluating the captured responses

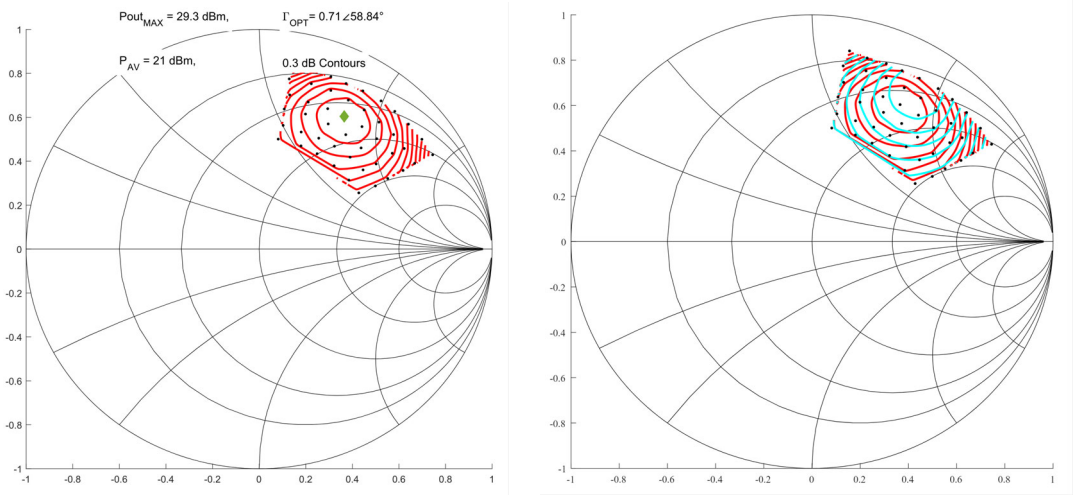

(a) (b)

Figure 3.4: LP data illustration of a GaN on SiC HEMT structure device at 10 GHz. Power contours with 0.3 dB of contours level (a), illustration of the power and DCRF efficiency contours (b).

of multiple variables, achieved by overlaying contours on the Smith Chart. The key lies in striking a reasonable compromise between these contours. This process allows one to identify the optimum load conditions that simultaneously optimise desired performance metrics, such as maximising power output while maintaining high efficiency, as illustrated in Figure 3.4b. The experimental data was obtained from a GaN-on-SiC HEMT device configured in amplifier mode at 10 GHz.

The quality of the LP systems and extracted data will often be parametrised through factors such as;

- *Repeatability*; high accuracy in recapturing the reflection coefficient is one of the most critical factors in LP measurement systems, facilitating more precise applications.
- *Tuning range*, extensive tuning range closer to open and short circuits on the Smith Chart.
- *Resolution*; higher number of measurement points to satisfy applications highly sensitive to impedance variations, albeit at the cost of increased measurement time.
- *High power handling*; LP systems capable of delivering high power levels can produce more reliable measurement data around the nonlinearity point of the DUT.

Figure 3.1 asserts that Γ_{L} can be synthesised by using the load tuner to either adjust the phase and magnitude of the reflected wave A_2 or change the load impedance Z_L. This principle forms the basis of the two main LP measurement system techniques and setups: the passive setup, which employs a passive tuner to adjust Z_L, and the active setup, which involves feeding electronically modified reflected wave to the output port of the DUT.

3.1.3 Passive Load-Pull System

As the name implies, a load-pull system is referred to as passive when load impedance variations are exercised using a passive tuner. Passive tuners are utilised with peripheral instruments and components, such as a vector network analyser (VNA), directional couplers, bias tees, and isolators, Figure 3.5 depicts a passive LP system's most basic block

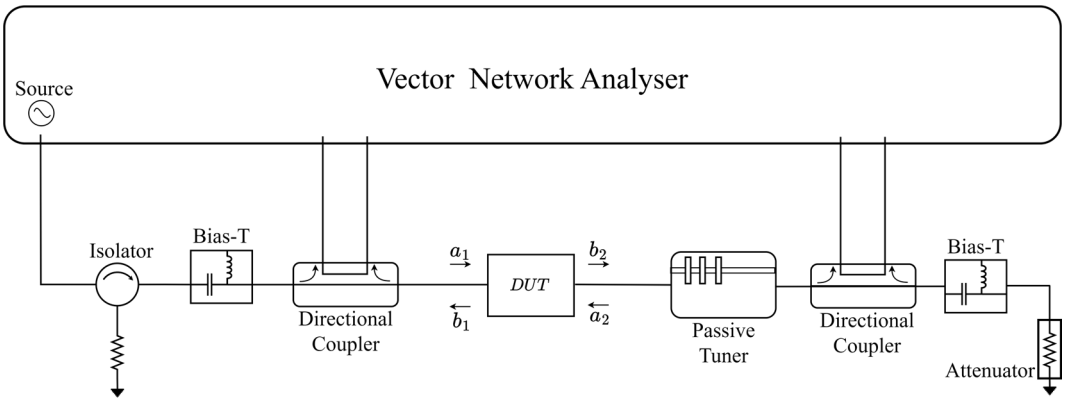

Figure 3.5: A generic block diagram of a passive load-pull system.

diagram. Additional components can be integrated to meet the specific requirements of the measurement. For example, employing a passive tuner at the DUT's input to utilise the source-pull function can significantly enhance the versatility of the measurement system.

The two primary types of passive tuners are the electromechanical tuner (EMT) and the electronic tuner (ETS), each of which has its own limitations. The passive EMT consists of a stub, slug, or screw-type probe vertically positioned above a horizontal transmission line. These probes, also known as mismatched elements, move vertically and horizontally along the transmission line to introduce mismatches or, in other words, to change the impedance. The movement of the stub in the Y and X-directions alters the magnitude and phase of the mismatch, respectively [5].

Figure 3.6 visually demonstrates how single-stub EMTs work. When the stub does not interfere with the electric field of the propagating travelling wave, the signal encounters a 50 Ω load, which is the predetermined matched termination with minimal impact from the transmission line, as shown in Figure 3.6a. As the stub moves in the Y-direction towards the centre of the transmission line, it increases the magnitude of the reflection coefficient at the reference plane, as illustrated in Figure 3.6b. The phase of the reflection coefficients can be adjusted by the horizontal (X-direction) movement along the transmission line, as depicted in Figure 3.6c. A passive tuner with small incremental movements of the stub in the X and Y directions, often in the range of microns, is known as a high-resolution tuner.

It was previously highlighted that uncontrolled harmonics can significantly impact device performance. These dynamically varying harmonics alter the optimal impedance at

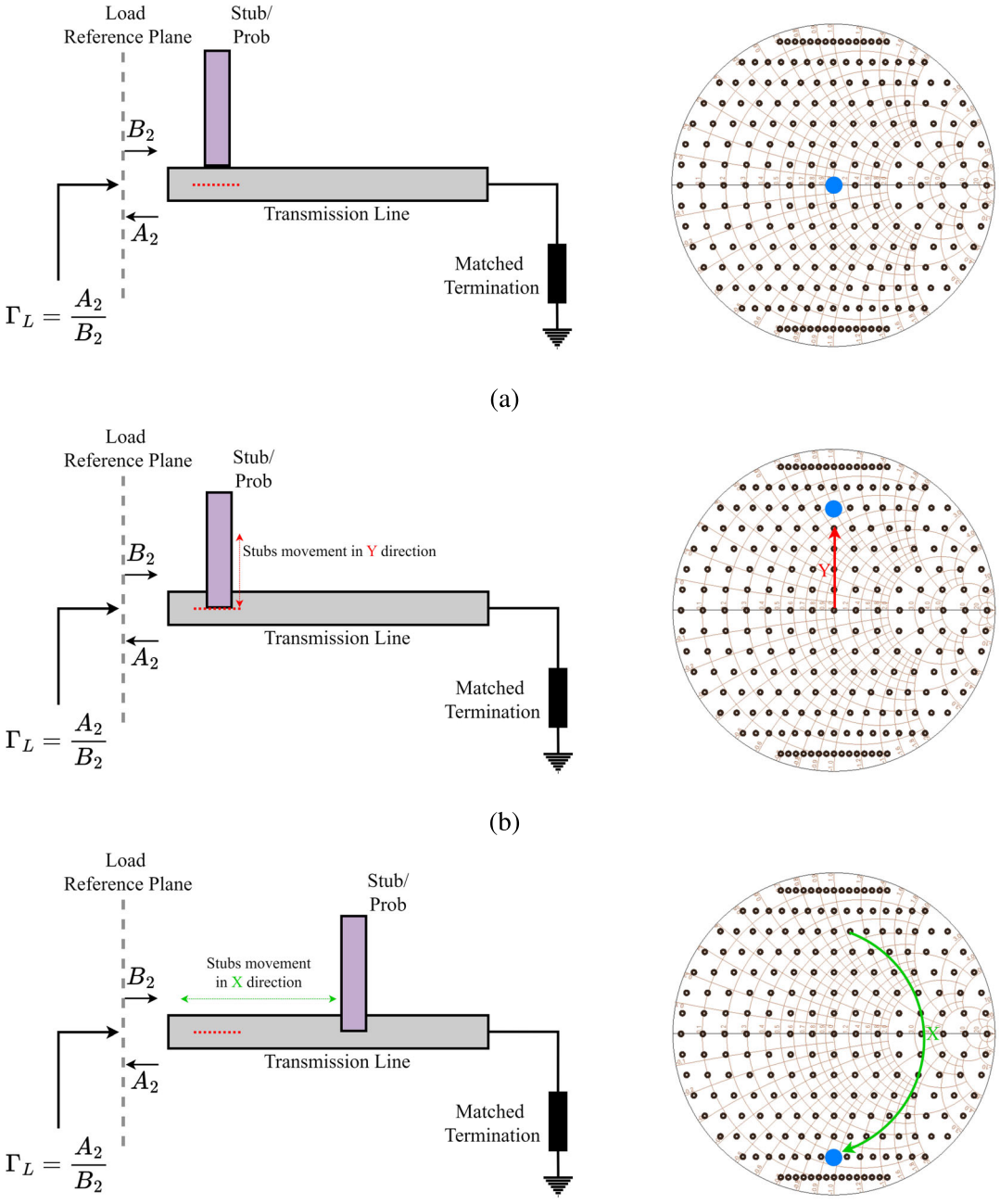

Figure 3.6: A representation of an EMT in a matched condition (a), Manipulating the magnitude of the Γ_L by stub's movement in Y-direction (b), Manipulating the phase of the Γ_L by stub's movement in X-direction (c). Note: The depiction of the stub's movement and load impedance (blue circle) on the Smith Chart is intended to show their general functional relationship; therefore, they are inaccurate.

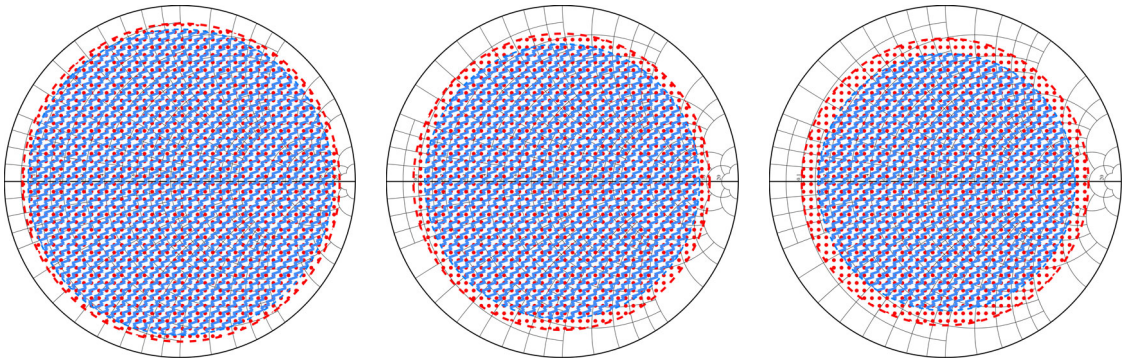

(a) (b) (c)

Figure 3.7: Tuning coverage comparison of triplexer based harmonic load-pull (coloured in blue) and *multipurpose single tuner three-harmonics load-pull* (coloured in red) at the fundamental frequency (a), 2nd harmonic (b), and 3rd harmonic (c).

the load terminal's fundamental frequency. If impedance fluctuates without user control or cannot be stabilised for varying harmonic impedances, the obtained measurement results would be considered invalid. This concern underscores the importance of considering harmonics during LP characterisation. Beyond harmonically tuned devices, enhancements can be achieved by identifying optimal loading conditions for harmonic impedance terminations rather than the conventional 50 Ω. According to [5], there are three primary passive harmonic LP architectures: triplexer-based harmonic load-pull, harmonic rejection tuner harmonic load-pull, and multipurpose single-tuner harmonic load-pull.

The earlier architecture exhibits limited tuning coverage due to the inherent losses of multiple passive tuners and additional components, such as the triplexer. In contrast, the latest configuration eliminates the losses related to supplementary passive tuners, resulting in enhanced reflection coefficient tuning coverage. A three-harmonic single tuner harmonic load-pull can be implemented using the same passive tuner depicted in Figure 3.6, equipped with three independent vertical stubs to independently control the magnitude and phase of the reflection coefficients at three harmonic frequencies: F_0, $2F_0$, and $3F_0$. Figure 3.7 illustrates the Γ_L tuning coverage difference between the triplexer-based harmonic load-pull and the multipurpose single tuner harmonic load-pull at the passive tuner reference plane.

Nonetheless, although theoretically, the ideal Γ_L defined on the Smith Chart is expected to be $|\Gamma_L| = 1$, in practice at the tuner reference plane, Γ_L is less than 1. The additional loss originating from the tuner and the accompanying instrumentation causes this value to

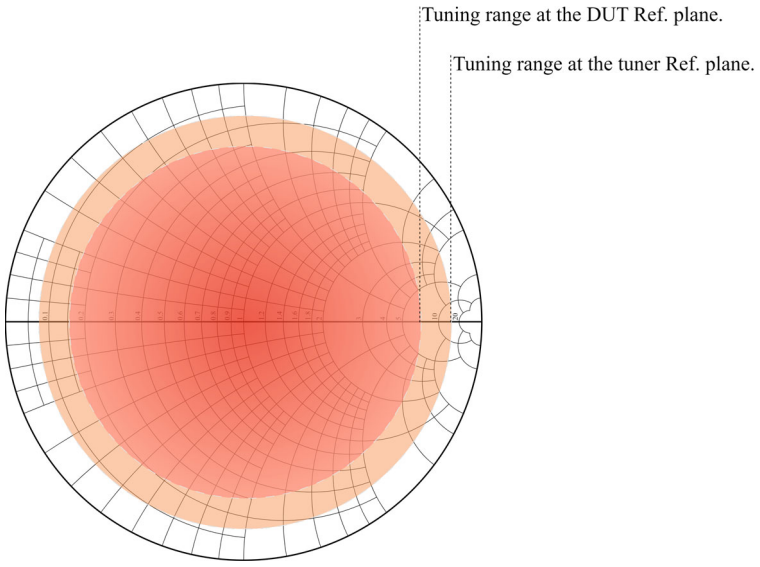

Figure 3.8: *Single tuner load-pull system* tuning coverage illustration at tuner reference plane and the DUT's reference plane.

decrease further at the DUT's reference planes.

Figure 3.8 provides an approximate representation of the expected tuning range from a passive LP system at different reference planes.

The shortcomings mentioned above underscore the necessity of solutions for applications operating in highly reflective impedance environments, such as high-power devices, PAs and harmonic measurements. While passive solutions are available and discussed by [6], active LP architecture offers a superior alternative by eliminating the losses associated with the use of passive tuners, thereby addressing these limitations more effectively.

3.1.4 Active Load-Pull System

Active LP is a more sophisticated technique compared to its passive counterpart, offering more extensive tuning coverage and higher resolution in load definition. The principles of active LP can be clarified by referencing Figure 3.1. This figure demonstrates that an alternative method for calculating Γ_L involves measuring the incident and reflected travelling waves (A_2, B_2) at the load terminal. Equation (3.6) demonstrates that the same concept also applies to harmonics.

$$\Gamma_{L,h} = \frac{A_{2,h}}{B_{2,h}} \tag{3.6}$$

Therefore, the incident wave $A_{2,h}$ at the output port can be injected by the user to generate predefined sets of $\Gamma_{L,h}$ at the DUT reference plane and actively adjusted to achieve the desired reflection coefficients. This approach ensures precise impedance control, thereby enhancing the accuracy and efficiency of the device characterisation process. Given the above information, it is evident that active LP is utilised in applications requiring higher Γ_L values (note: a $|\Gamma_L| > 1$ can even be generated using an active LP). While various active LP architectures are reported, such as feed-forward active LP in which a portion of the input signal is used to generate a coherent modified signal that is reflected at the DUT plane [7, 8], the two well-known active LP architectures are closed-loop and open-loop.

3.1.5 Close Loop Active Load-Pull Measurement

Figure 3.9 illustrates a block diagram at which the desired load reflection coefficient Γ_L can be obtained by sampling the incident travelling wave B_2 and injecting it back as reflected travelling wave A_2 at the output port into the DUT after required amplification and phase shift [9]. Therefore, Γ_L can be rewritten based on applied modification on B_2 using the complex variable $\rho.e^{j\theta}$, where, ρ is the magnitude and θ is the phase, as Equation 3.7. Thus, the load reflection coefficient (Γ_L) at the DUT reference plane depicted in Figure 3.9, given by Equation 3.7 can be set to any value (even larger than unity).

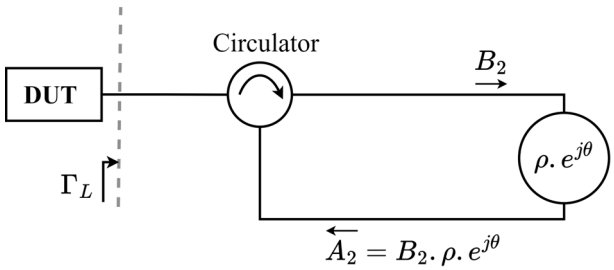

Figure 3.9: Load reflection coefficient synthesis with employment of complex variable $\rho.e^{j\theta}$ for magnitude and phase modifications.

$$\Gamma_L = \frac{A_2}{B_2} = \frac{B_2 \cdot \rho \cdot e^{j\theta}}{B_2} = \rho \cdot e^{j\theta} \tag{3.7}$$

To establish a generic system capable of the magnitude and phase modifications mentioned in 3.7, a circulator is necessary to direct the incident and reflected travelling

waves to their respective paths. Additionally, a variable attenuator and a loop amplifier are required for magnitude modification, along with a variable phase shifter for phase adjustment, as depicted in Figure 3.10.

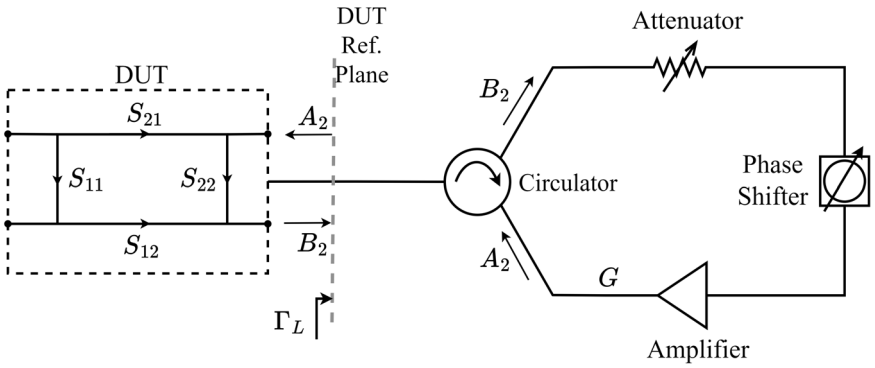

Figure 3.10: A block diagram of a generic closed-loop active LP with circulator, variable attenuator, variable phase shifter and a loop amplifier.

Assuming the newly modified magnitude by variable attenuator and loop amplifier as the G as in 3.10, in favour of practical implementations and in order to maintain stability, the G should be smaller than the return loss at the output port of the DUT as expresses in Equation 3.8.

$$\mathrm{G} < 20 \log |S_{22}| \text{ dB} \tag{3.8}$$

Further analysing the shortcomings of such architectures is that they can cause high loop oscillations if the loop amplifier's gain exceeds the isolations of the circulator [10]. These bottlenecks are addressed by using an isolator after the amplifier. Furthermore, more improvement can obtained by employing a band-pass filter prior to the amplifier to filter out oscillations outside the frequency band [6].

3.1.6 Open Loop Active Load-Pull Measurement

Active open-loop load pull, similar to the closed-loop configuration, involves injecting a signal back into the output port of the DUT. While in the closed-loop setup, the injected signal is sampled from the B_2 component, in the open-loop setup, the injected signal comes from an external signal generator. In open-loop LP, there are two separate sources for

excitations: one providing the input signal to the DUT and the other injecting a signal to synthesise Γ_L at the output port of the DUT. Both sources must be locked to a common reference signal to maintain phase coherence.

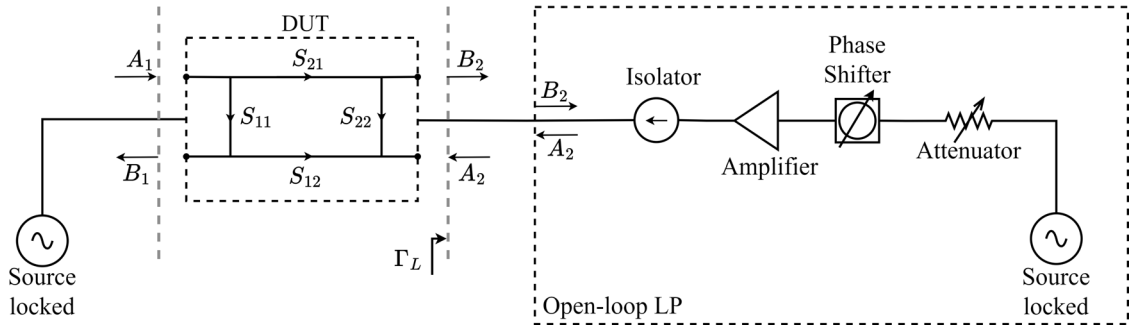

Figure 3.11: A block diagram of a generic open-loop active LP with simplified signal flow graph of DUT.

Figure 3.11 shows the use of components in setting up a straightforward open-loop system. The fact that the injecting signal A_2 is not derived from the B_2 implies that the DUT significantly influences the synthesis of load reflection coefficients [11–13], necessitating an iterative process to obtain a satisfactory definition of Γ_L. In this configuration, Γ_L can be expressed at the DUT's reference plane as in Equation 3.9.

$$\Gamma_L = \frac{A_2}{B_2} = \frac{A_2}{S_{21}\,A_1 + S_{22}\,A_2} = \frac{1}{S_{21}\,\frac{A_1}{A_2} + S_{22}} \tag{3.9}$$

where large-signal S_{21} and S_{22} are the extracted components from the DUT at the fundamental frequency.

Equation 3.9 implies that injecting A_2 component alone is capable of defining a range of 0 to ∞ for the load reflection coefficients. The load reflection coefficient will be zero when $A_2 = 0$. As the A_2 component increases, the first term in the denominator decreases until it becomes zero, leaving the term $1/S_{22}$, which implies that Γ_L can reach infinity depending on the component values.

To outline the advantages of the open-loop LP, its high stability can be noted, attributed to the absence of loop oscillations since there is no feedback loop. Additionally, it offers the capability of achieving higher magnitudes of reflection and can be easily extended to a multi-harmonic setup.

Multi-harmonic open-loop active LP can be executed by employing a *Triplexer* to combine the components of generating A_2 corresponding to the fundamental frequency F_0 and its harmonics (for instance, in a 3-harmonics setup, these would be $A_2(F_0)$, $A_2(2F_0)$, and $A_2(3F_0)$. As with the previous configuration, the sources must be locked to a common reference to maintain phase coherence. Figure 3.12 illustrates a block diagram of a 3-harmonics active open-loop LP setup, where the magnitude and phase adjustment can also be performed through built-in functions in the corresponding signal generator or separate components of the attenuator and phase shifter [14].

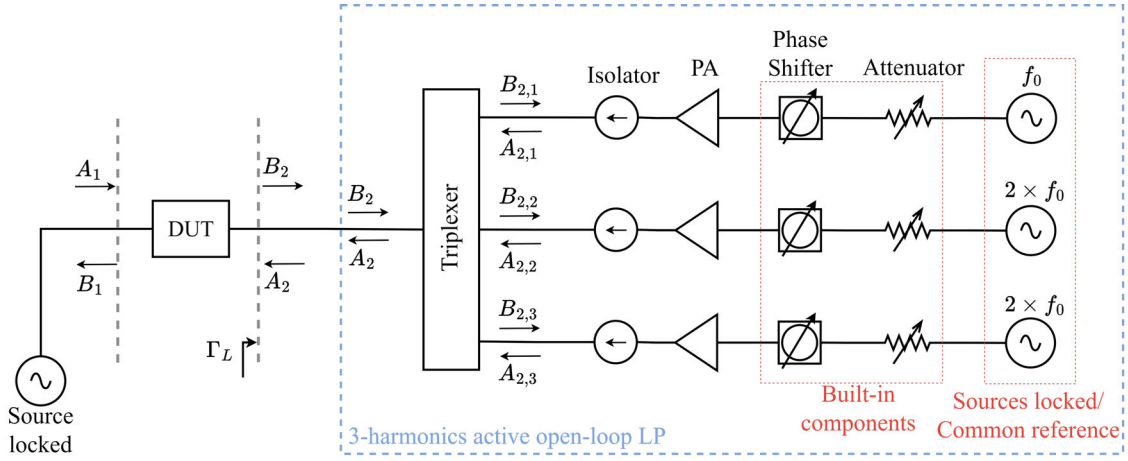

Figure 3.12: A block diagram of a 3-Harmonics active open-loop active LP with three signal generators locked to the common reference.

The main limitation of an active open-loop harmonic load-pull system is the high cost of scaling to higher harmonics due to expensive load-pull instruments. This can be addressed by using a load-pull source accountable for multi-harmonic components generation or employing doublers and triplers with a power divider. However, this increases the required output power from loop amplifiers. Furthermore, harmonic active open-loop load-pull setups cannot independently synthesise harmonic reflection coefficients due to interactions between different harmonic components of A_2 or B_2, which disrupt the specifications of other reflection coefficients during convergence [15].

3.2 Behavioural Modelling

In the course of active device development, remarkable progress has been made since the 1940s and 1950s, when the first physical transistor models were introduced to streamline design iterations and simplify the prototyping process [16]. As the name suggests, physical models are fundamentally based on the underlying physics of the technology rather than electrical circuit assumptions, making them particularly effective at the device level. Several fundamental equations, including but not limited to drift-diffusion equations for charge transport, Poisson's equation for electrostatic potential, and continuity equations for charge conservation, are used to describe physical behaviours and material properties. These models offer a detailed and accurate representation of a transistor's intrinsic behaviour. The inability to efficiently represent high-frequency non-linear behaviours as well as scalability challenges in modelling emerging large-scale integrated circuits (ICs) highlighted the primary bottleneck of physical models. To address these limitations, engineers developed compact models as a practical solution, enabling CAD for large-scale integrated circuits [17]. Compact models utilise empirical and physical parameters to predict the performance of transistors, typically based on measured DC / pulsed *IV* and scattering parameters. Given the assumption of an electrical circuit model, these models account for non-linearities and parasitic effects at the die level. However, to ensure a more accurate and reliable simulation, package-level modelling is often required in addition to die-level modelling.

Advancements in modelling have found it more efficient to bypass the limitations imposed by extensive physics-based calculations and electrical circuit assumptions, which are often constrained to die-level models. This progress led to the rise of behavioural models [18], which rely on measured data as input signals to predict the response at the output. This method treats the entire device, including bonds and packaging, as a black box, eliminating the need for detailed knowledge of the device's internal physics while accounting for the non-linear behaviour in high-power, saturated conditions. Figure 3.13 presents a detailed comparison of the trade-offs across the three main transistor modelling techniques of the *Physical* model, *Compact* model and *Behavioural* model.

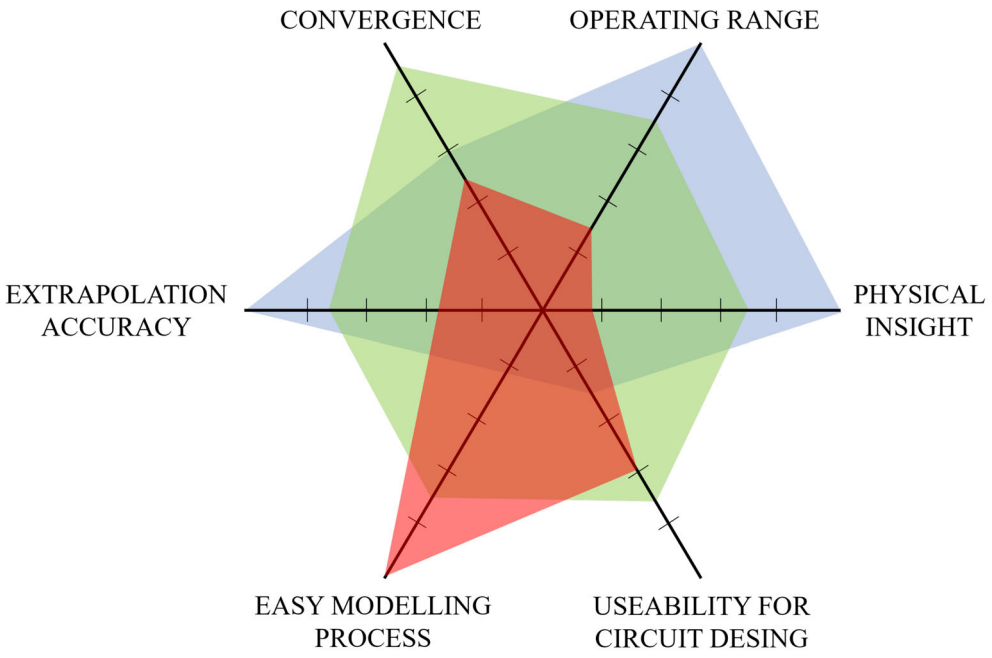

Figure 3.13: Comparison of the characteristics of the three primary transistor modelling techniques: Physical model (light blue), Compact model (light green), and Behavioural model (light red) [19].

3.2.1 Non-Linear Behavioural Modelling

In general, S-parameters are among the earliest and simplest behavioural models, relying on measured data to model the behaviour of components and represent their equivalent electrical circuits. However, predicting the non-linear behaviour of a component based on data extracted under linear conditions proves inefficient. The advent of non-linear network analysers, with their ability to perform accurate and reliable large-signal characterisation, has paved the way for the development of advanced behavioural modelling applications.

Behavioural models rely on measurement data and the application of mathematical functions to identify model parameters derived from port information obtained during nonlinear measurements. These models effectively represent both the linear and nonlinear characteristics of a device with high accuracy. A significant advantage of behavioural modelling lies in its ability to streamline the design process by delivering essential data while safeguarding the vendor's intellectual property, as the extraction process does not require an understanding of the device's internal structure or equivalent circuit.

The key challenge and ongoing development in behavioural models are centred on

refining the "describing mathematical functions". These behavioural models focused on enhancing computational efficiency with a minimal number of model coefficients (input) without sacrificing model accuracy, allowing for more practical application across a wide range of devices. Building on the brief overview provided above, the next sections of this chapter will outline the most commonly utilised models in chronological order of behavioural model developments, offering a foundational understanding of the modelling approaches applied in this work.

3.2.2 HOT S-PARAMETERS

Hot S-parameter, also known as large-signal S-parameter, were introduced to extend and implement the concept of conventional S-parameter into the domain of non-linear devices operating under large-signal conditions by means of two distinct excitations of large and small signals. The large signal is the primary excitation that drives the device into non-linear operation. This large signal is typically at a carrier frequency (denoted as f_c), which alters the device's operating state, introducing non-linearities such as harmonic distortion and gain compression. The small signal (f_s) is superimposed on top of the large signal. The equations below are modifications of conventional S-parameter, accounting for the large-signal environment.

$$HotS_{ij} = \frac{b_i(f_s)}{a_j(f_s)} \tag{3.10}$$

As detailed in [20, 21] the hot S-parameter models allow for quick evaluations of device behaviour with the use of conventional network analysers. To account for large signal tone (f_c) non-linearities the Equation 3.10 can be modified as

$$\begin{bmatrix} b_1(f_c) \\ b_2(f_c) \end{bmatrix} = \begin{bmatrix} \mathrm{Hot}S_{11} & \mathrm{Hot}S_{12} \\ \mathrm{Hot}S_{21} & \mathrm{Hot}S_{22} \end{bmatrix} \begin{bmatrix} a_1(f_c) \\ a_2(f_c) \end{bmatrix} \tag{3.11}$$

In Equation 3.11, the hot S-parameters depend on both the amplitude and frequency of the large signal $a_1(f_c)$, which introduces a non-linear relationship. However, some inaccuracies may arise when using Equation 3.11 to model the non-linear output matching

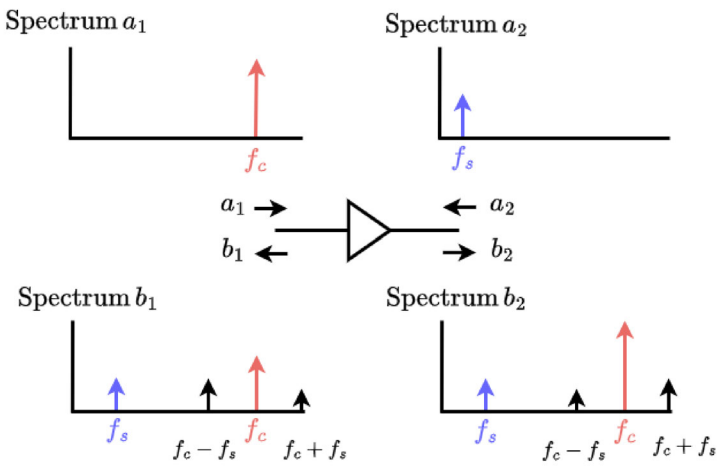

Figure 3.14: Hot S-parameter representation.

characteristics (HotS_{22}) and non-linear isolation characteristics (HotS_{12}). These inaccuracies are due to the absence of the conjugate product of the $a_2(f_c)$ tone. The Hot-S parameters that account for distortion characteristics are formulated by [22] as shown in the following equation.

$$\begin{bmatrix} b_1(f_c) \\ b_2(f_c) \end{bmatrix} = \begin{bmatrix} \text{Hot}S_{11} & \text{Hot}S_{12} \\ \text{Hot}S_{21} & \text{Hot}S_{22} \end{bmatrix} \begin{bmatrix} a_1(f_c) \\ a_2(f_c) \end{bmatrix} + \begin{bmatrix} T_{12} \\ T_{22} \end{bmatrix} e^{j2\varphi(a_1(f_c))} \text{conj}(a_2(f_c)) \tag{3.12}$$

The terms T12 and T22 refer to the non-linear response of the disturbance signal and its conjugate term near the working point of the large signal.

3.2.3 Poly-Harmonics Distortion Modelling

A poly harmonic distortion (PHD) model can be derived by externally stimulating the inputs of the DUT and measuring its output response. This approach requires a narrowband stimulus signal at the dominant fundamental frequency, augmented by relatively small, harmonically related discrete tones. By employing this method, a wide range of non-linear characteristics—including the amplitude and phase of harmonics, compression behaviour, amplitude modulation (AM)- phase modulation (PM) conversion, spectral regrowth, and amplitude-dependent input and output matching—can be accurately characterised. These

insights are obtained by connecting the DUT to a large signal network analyser (LSNA) and applying the PHD model [23].

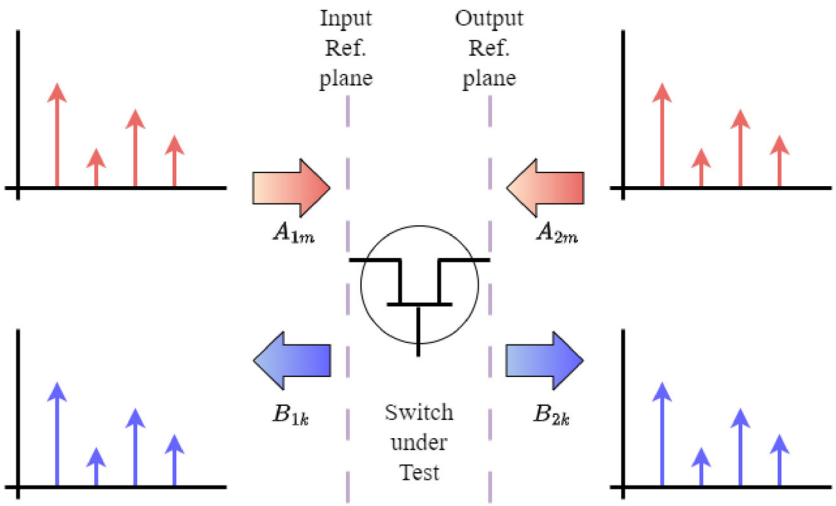

Figure 3.15: The concept of the describing function adapted from [23] with modifications.

$$\begin{aligned} B_{1k} &= F_{1k}(A_{11}, A_{12}, \ldots, A_{21}, A_{22}, \ldots) \\ B_{2k} &= F_{2k}(A_{11}, A_{12}, \ldots, A_{21}, A_{22}, \ldots) \end{aligned} \tag{3.13}$$

Unlike physical models, and similar to S-parameters, the basic quantities in PHD models are normalised travelling voltage waves, as introduced by Pozar. This approach is more convenient, as most modern measurement systems and non-linear vector network analyser (NVNA) instrumentation inherently operate in the domain of incident waves (A-waves) and scattered waves, commonly referred to as B-waves.

The PHD model operates on the assumption of discrete tone signals (multisines) that are periodic in nature. In other words, it considers narrowband modulated versions of a dominant fundamental frequency (F_0) as harmonics, with indices describing components such as 0: DC, 1: -F_0, 2: 2*F_0, 3: -3*F_0, and so on. A general mathematical framework in the frequency domain, commonly referred to as the "describing function" [24, 25], can be applied to a given DUT. This framework determines a set of multivariate complex functions, $F_{ph}(.)$, that establish the correlation between all relevant input spectral components, A_{ph}, and the corresponding output spectral components, B_{ph}. While the concept is mathematically formulated in Equation 3.14, it is also visually represented in Figure 3.15 for better understanding.

$$B_{ph} = F_{ph}(A_{10}, A_{11}, A_{12}, \ldots, A_{20}, A_{21}, A_{22}, \ldots, A_{ph}) \tag{3.14}$$

The indices p signify the port numbers, ranging from one to the total number of available ports in the system. Meanwhile, the subscript h identifies the harmonic order, starting from 0 (representing DC) and extending to the maximum harmonic component (n*F) captured during the analysis.

As mentioned, Equation 3.14 represents a general form that lacks the time-invariant property. This limitation means that the function $F_{ph}(.)$ cannot fully describe the relationship between the incident A_{ph}-waves and the scattered B_{ph}-waves. Since, in the frequency domain, a time delay corresponds to a linear phase shift proportional to the frequency, the equation is generalised by incorporating the phase component to account for this behaviour in non-linear systems.

$$B_{ph}e^{jh\theta} = F_{ph}(\mathrm{DC}, A_{ph}e^{jh\theta}) \tag{3.15}$$

The incident travelling wave at port 1, corresponding to the fundamental tone (A_{11}), serves as the dominant large-signal component, while all other harmonics are considered narrowband modulated components of $\mathrm{F_0}$. This is referred to as the harmonic superposition principle [26], which holds true for most power transistors and power amplifier applications driven by narrowband input signals, as illustrated in Figure 3.16. Consequently, all harmonics can be phase-normalised to the A_{11} incident signal to further reduce complexity. This approach can be formalised as Equation. 3.17 by the introduction of the phasor, $P = \angle A_{11}$. The benefit of Equation 3.14, compared to Equation 3.17, is that the first input argument is always a positive real number rather than a complex number (amplitude of the fundamental component at input port 1).

$$P = e^{+j\theta(A_{11})} \tag{3.16}$$

$$B_{ph} = F_{ph}(|A_{11}|, A_{12}P^{-2}, A_{13}P^{-3}, \ldots, A_{21}P^{-1}, A_{22}P^{-2}, \ldots)P^{+h} \tag{3.17}$$

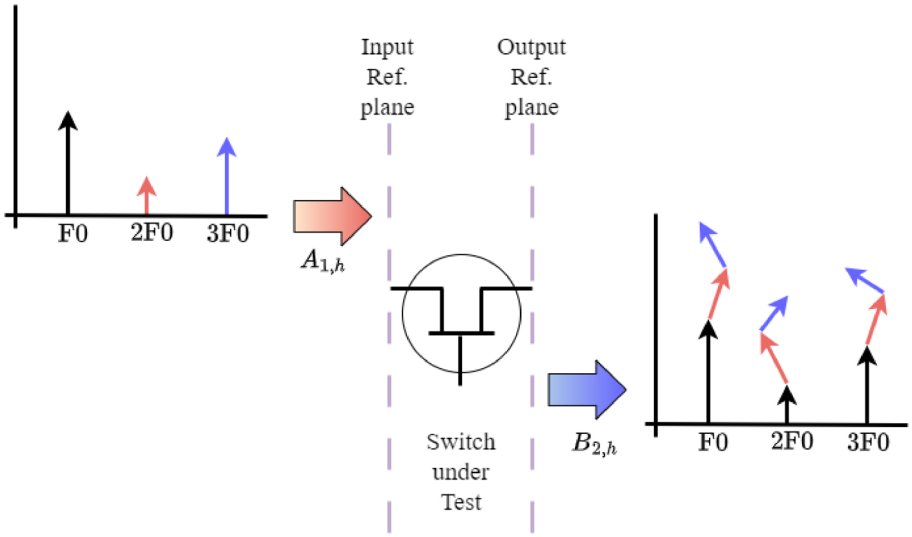

Figure 3.16: Harmonic superposition principle adapted from [23], with modifications.

As shown in Figure 3.16, the injection of the fundamental signal (A_{11}) at the input generates harmonic components at the output, represented by black arrows. With F_0 held constant, introducing a second input component (A_{12}) induces relative deviations in each individual harmonic of F_0 within the output spectrum (B_2), illustrated by red arrows. Similarly, the injection of a third component produces deviations depicted by green arrows. The harmonic superposition principle has been demonstrated to hold even under highly nonlinear operating conditions. Incorporating this principle, Equation 3.17 is refined to yield Equation 3.18.

$$B_{p,h} = \sum_{q,n} S_{pq,nh}\left(|A_{11}|\right) P^{+h-n} A_{q,n} + \sum_{q,n} T_{pq,nh}\left(|A_{11}|\right) P^{+h+n} \mathrm{conj}(A_{q,n}) \tag{3.18}$$

Similar to the indices p and h in the output spectrum, the subscripts q and n represent the port and harmonic indices, respectively, but correspond to the incident waves in the input spectrum. Consequently, the terms P^{+h-n} and P^{+h+n} capture the relative phase shifts arising from the non-linear interactions of the incident waves across harmonics h and n. The parameter $S_{pq,nh}$ denotes the non-linear scattering function [27] associated with the forward interaction between the input wave ($A_{q,n}$) and the resulting output wave ($B_{p,h}$). This scattering function depends on the magnitude of the fundamental tone ($|A_{11}|$) and determines how the system translates input magnitudes and phases into output

waves. Similarly, the parameter $T_{pq,nh}$ represents the non-linear scattering function for the conjugated components of the input waves (conj($A_{q,n}$)).

The describing function in 3.17 offers broad applicability but introduces significant complexity, as the device response depends on the non-linear interactions of stimulus phasors at all ports. To address this, non-linear network parameters (X-parameters) and the Cardiff model, inspired by PHD modelling, utilise truncated polynomial formulations to reduce the number of coefficients, making them practical for limited large signal operating points.

3.2.4 X-Parameters

In advancing non-linear measurements, Agilent introduced X-parameters an expanded version of S-parameter as a solution to address non-linear characteristics [28]. They developed a precision network analyser (PNA) equipped with firmware capable of transforming a standard VNA into an NVNA, enabling the measurement of vector-corrected absolute amplitudes and cross-frequency phase responses of a device under test. This innovation included a phase reference that allowed for precise vector-corrected cross-frequency phase measurements with narrow grid spacing. With the amplitude and cross-frequency phase data for all frequency spectra accurately captured, an inverse Fourier transform could then be applied to convert the frequency-domain data into time-domain waveforms.

These vector-corrected stimulus/response measurements form the basis for automated X-parameter characterisation. For a two-port component, X-parameter measurements require two signal sources. The precision network analyser extended (PNA-X) hardware architecture addresses this need by incorporating integrated "spectrally pure" sources, internal pulse modulators/generators, an internal combining network, and flexible signal routing capabilities. Additionally, the NVNA functions as a vector-corrected time-domain oscilloscope, measuring absolute signal amplitudes and cross-frequency phases with error correction applied. This time-domain data enables the analysis of voltage and current waveforms at the device terminals, facilitating the investigation of both linear and non-linear characteristics of the component.

Agilent enhanced the X-parameter measurement capabilities by introducing arbitrary load-dependent X-parameters for both fundamental and harmonic frequencies to the NVNA. The complete complex Γ-dependence of a device under large-signal operating conditions can now be captured and exported to simulation software, enabling accurate representation of devices using X-parameter models from device level to cascaded multi-stage amplifiers, Doherty configurations, or other complex amplifier circuit simulations.

In terms of theory and formulation, X-parameters adopt the same harmonic superposition principle as PHD modelling but are implemented within a restructured framework, as shown in Equation 3.19. Here, the device response $B_{p,h}$ is assumed to be linearly dependent on the stimuli $A_{q,l\neq1,1}$ and their conjugates (denoted by the asterisk, $*$), centred around the dominant large signal component $A_{1,1}$.

$$\begin{aligned} B_{p,h} = {} & (\angle A_{1,1})^{h} \cdot X^{(F)}_{p,h}(\mathrm{DC}, |A_{1,1}|) \\ \ldots, \quad & + \sum_{(q,l)} X^{(S)}_{p,h,q,l}(\mathrm{DC}, |A_{1,1}|) \cdot A_{q,l} \cdot (\angle A_{1,1})^{h-l} \\ \ldots, \quad & + \sum_{(q,l)} X^{(T)}_{p,h,q,l}(\mathrm{DC}, |A_{1,1}|) \cdot A^{*}_{q,l} \cdot (\angle A_{1,1})^{h+l} \end{aligned} \tag{3.19}$$

The subscripts 'p' and 'p' correspond to the respective port and harmonic index of the response B, while 'q' and 'l' represent the respective port and harmonic index of the stimulus A. Function $X^{(F)}_{p,h}$ describes the direct non-linear dependence of the response $B_{p,h}$ on the dominant large-signal component $A_{1,1}$. The $X^{(S)}_{p,h,q,l}$ set captures the forward interactions of the input spectral components $A_{q,l}$ with the response, whereas $X^{(T)}_{p,h,q,l}$ accounts for the contributions of the conjugated input spectral components $\mathrm{conj}(A_{q,l})$ to the response. Together, these components represent the complex non-linear relationships between the input and output spectral components under large-signal operating conditions.

3.2.5 TABLE-BASED CARDIFF MODEL

The Cardiff model's initial framework was introduced in 2005 as a lookup table-based model, referred to as the direct wave look up table (DWLUT) [29, 30]. As depicted in Figure 3.17, this model relied on extrinsic time-domain measured voltage and current waveforms to describe the $I_p(t)$ as in Equation. (3.20).

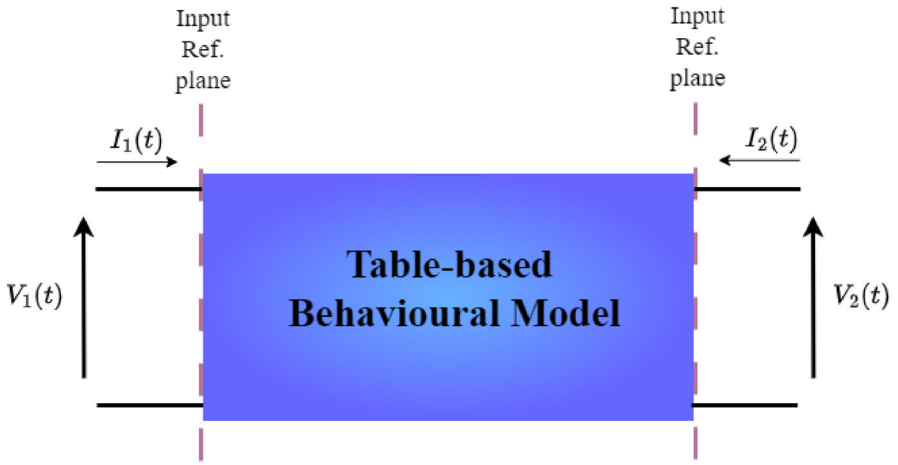

Figure 3.17: A block diagram to explain the table-based behavioural model.

$$I_p(t) = I_{p,DC} + \sum_{h=1}^{h} Y_{p,h}(hf_0)V_p^h(t) \tag{3.20}$$

Here, p represents the port number, and the harmonic components are indexed by h, with v expressed as shown in Equation. (3.21).

$$V_p(t) = |V_p|e^{j\theta}e^{j\omega t} \tag{3.21}$$

By applying the general principles governing Y-Parameters in a two-port network, the relationship between current and voltage components can be derived, as shown in Equation (3.22).

$$Y_{p,h}(hf_0) = F_1\left(|V_1|, \Gamma_{\text{LOAD}}, V_{1\text{DC}}, V_{2\text{DC}}\right) \tag{3.22}$$

At each harmonic (h), the admittance parameter $Y_{p,h}$ is characterised as a dependent function of several key factors: the magnitude of the input stimulus voltage ($|V_1|$), the

complex impedance of the applied load (Γ_{LOAD}), and the specific biasing conditions provided by the DC voltage levels (V_{1DC} and V_{2DC}).

In 2006, the model's formulation was enhanced to enable more precise integration of load-pull data into non-linear CAD simulators [31]. By 2008, as described in Equation 3.23, the model was further refined to allow for the rapid extraction of RF waves in the "A" and "B" domains, specifically tailored for fundamental frequency load-pull measurement data [32].

$$B_{p,h} = (\angle A_{1,1})^h \cdot K_{p,h}\left(|A_{1,1}|, DC, |A_{2,1}|, \frac{\angle A_{2,1}}{\angle A_{1,1}}, f_0\right) \tag{3.23}$$

The $K_{p,h}$ known as model coefficients are defined as lookup parameters that are normalised relative to the phase of the input stimulus $\angle A_{1,1}$. These coefficients are indexed using several critical parameters that describe the device's behaviour under large-signal operation. These include the fundamental frequency (F_0), the magnitude of the output stimulus signal $|A_{2,1}|$, the phase of the output stimulus signal $\angle A_{2,1}$, and the applied DC bias. In essence, it was not true behavioural model, as its primary purpose was solely to make non-linear data accessible for CAD tools. The major limitation of this approach was its inability to predict beyond the specific measurements it was derived from.

3.2.6 Cardiff Behavioural Model

To overcome the limitations of multiple measurement iterations, extensive lookup indexing, and restricted application, as well as to incorporate the capability of predicting true non-linear behaviour through interpolation and extrapolation, Cardiff's DWLUT evolved into the Cardiff behavioural model.

The Cardiff behavioural model's mathematical foundation is polynomial-based and aligns closely with the original PHD model. However, it distinguishes itself from the X-parameters model by utilising mixing theory instead of harmonic superposition. This approach acknowledges that when multiple continuous waves (CW) harmonically related stimuli are introduced into a multi-port non-linear system, they interact, or "mix," to produce complex responses. As part of its development, the Cardiff behavioural model

formulation was refined to eliminate the phasor vector from the indexing parameters, as demonstrated in Equation 3.24.

$$B_{p,h} = (\angle A_{1,1})^h \sum_{n=-(w-1)/2}^{+(w+1)/2} K_{p,h,n}\left(|A_{1,1}|, DC, |A_{2,1}|, f_0\right)\left(\frac{\angle A_{2,1}}{\angle A_{1,1}}\right)^n \tag{3.24}$$

The parameter w represents the mixing order and is directly utilised to determine the phase exponent n. Extending the model coefficients to account for the dependency on the magnitude of the output stimulus $|A_{2,1}|$. This advancement reduces the size of data tables by expressing the variation of $K_{p,h,n}$ as a function of $|A_{2,1}|$.

$$K_{p,h,n} = \sum_{m=|n|}^{m=|n|+2r} L_{p,h,m} \cdot |A_{2,1}|^m \tag{3.25}$$

Essentially, this approach generates the corresponding mixing matrix, which characterises the non-linear interactions resulting from the simultaneous excitation of the system by multiple stimuli. Removing the dependence of model coefficients on both the phase and magnitude of $|A_{2,1}|$, mathematically relates the device's output response directly to the input stimulus signals, which marked a significant breakthrough in the evolution of the Cardiff behavioural model's general formulation for fundamental load-pull only as Equation 3.26 [33–35].

$$\begin{aligned} B_{p,h} = (\angle A_{1,1})^h \sum_{r=0}^{r=(w-h)/2} \sum_{n=-((w-h)/2-r)}^{n=h+(w-h)/2} \ldots, \\ \ldots, K_{p,h,m,n}(|A_{1,1}|, DC, f_0)|A_{2,1}|^m \left(\frac{\angle A_{2,1}}{\angle A_{1,1}}\right)^n \end{aligned} \tag{3.26}$$

Where $m = |n| + 2r$, and the variable r serves as the magnitude indexing parameter. While the maximum value of r in Equation (3.26) is defined as $(w - h)/2$, its range is bounded between $r_{\min} = 0$ and $r_{\max} = 1$.

Further studies on the Cardiff model demonstrated that, at the intrinsic reference impedance of a device, the real components of the admittance domain (voltage and current) remain unaffected by frequency variations, while the imaginary components exhibit a linear dependence on frequency [36]. At the same time, most RF measurement systems,

including the Cardiff model, operate based on incident (A) and reflected (B) travelling waves. To address this limitation, [36] proposed a reformulated Cardiff model in the admittance domain alongside an *indirect* extraction methodology. This approach involves initially extracting the model coefficients in the A and B domains, then transferring the data into CAD software (such as Keysight's ADS) for "voltage load-pull" simulations (with $|V_{11}|$ held constant). The simulation outcomes are subsequently used to generate a refined admittance domain model.

Later, the inclusion of the $|V_{11}|$ variable into the Cardiff model's mathematical framework, as introduced by [37], eliminated the requirement for it to remain constant during the extraction process. This advancement enabled the direct extraction of the model's coefficients directly from load-pull measurement data. The Cardiff model formulation was subsequently adapted and expressed in the admittance domain, as shown in Equation (3.27), and in the A and B domain, as shown in Equation (3.28).

$$I_{p,h} = (\angle V_{1,1})^h \sum_{t=0}^{t=(w-h)/2} \sum_{r=0}^{r=(w-h)/2-t} \sum_{n=-((w-h)/2-r)}^{n=h+(w-h)/2} \ldots, \ldots, C_{p,h,m,n,x}(DC, f_0) \cdot |V_{1,1}|^x \cdot |v_{2,1}|^m \left(\frac{\angle V_{2,1}}{\angle V_{1,1}}\right)^n \tag{3.27}$$

$$A_{p,h} = (\angle A_{1,1})^h \sum_{t=0}^{t=(w-h)/2} \sum_{r=0}^{r=(w-h)/2-t} \sum_{n=-((w-h)/2-r)}^{n=h+(w-h)/2} \ldots, \ldots, M_{p,h,m,n,x}(DC, f_0) \cdot |A_{1,1}|^x \cdot |A_{2,1}|^m \cdot \left(\frac{\angle V_{2,1}}{\angle V_{1,1}}\right)^n \tag{3.28}$$

Where '$x = |h - n| + 2t$' and 't' is the magnitude restricting index parameter of $|V_{11}|$. The $C_{p,h,m,n,x}$ and $M_{p,h,m,n,x}$ are the general Cardiff model coefficients dependent on $|V_{11}|$ and $|A_{11}|$ for the admittance (I and V) and travelling wave (A and B) domains, respectively.

The Cardiff model, as represented in its generalised formulation in Equation (3.28), is inherently constrained by the dynamic range of $|A_{11}|$ that it is capable of modelling, which necessitated the use of distinct model coefficients to represent the device's behaviour across low, medium, and high power levels. An empirical investigation of load-pull measurement data under pulsed RF excitation, conducted by [38], resulted in a revised Cardiff model formulation as in Equation (3.29). This new approach integrates $|A_{11}|$ based on mixing

w=5th									
n	$t=0$			$t=1$			$t=2$		
	$r=0$	$r=1$	$r=2$	$r=0$	$r=1$	$r=2$	$r=0$	$r=1$	$r=2$
$n=-2$	5	∄	∄	∄	∄	∄	∄	∄	∄
$n=-1$	3	5	∄	5	∄	∄	∄	∄	∄
$n=0$	1	3	5	3	5	∄	5	∄	∄
$n=1$	1	3	5	3	5	∄	5	∄	∄
$n=2$	3	5	∄	5	∄	∄	∄	∄	∄
$n=3$	5	∄	∄	∄	∄	∄	∄	∄	∄

Table 3.1: Calculated model term orders for 5th,-order Cardiff model at the fundamental frequency ($h=1$). Term orders are computed using the formula: $order = |h-n| + |n| + 2t + 2r = m + x$. Wherever a model term does not exist, the symbol '∄' is used in the table. In practical applications, only the terms in black are typically used for model extraction, with the maximum values of 'r' and 't' often restricted to 1 ($r_{\max} = t_{\max} = 1$) [38].

theory principals, to cover the entire power sweep range using a single set of model coefficients, effectively eliminating the need for input drive level as a lookup indexing parameter.

$$B_{p,h} = (\angle A_{1,1})^h \sum_{t=0}^{t_{\max}} \sum_{r=0}^{r_{\max}} \sum_{n_{\min}}^{n_{\max}} M_{p,h,m,n,x} \cdot |A_{1,1}|^x \cdot |A_{2,1}|^m \cdot \left(\frac{\angle A_{2,1}}{\angle A_{1,1}}\right)^n \tag{3.29}$$

$$\begin{cases} t_{\max} = \frac{w-h}{2} \\ r_{\max} = \frac{w-h}{2} - t \\ n_{\min} = -\left(\frac{w-h}{2} - t - r\right) \\ n_{\max} = h + \left(\frac{w-h}{2} - t - r\right) \\ m = |n| + 2r \\ x = |h-n| + 2t \end{cases}$$

The indices 'p' and 'h' denote the port and harmonic indices, respectively, with 'h' referring to the fundamental frequency (F_0). The parameters 'm' and 'n' represent the magnitude and phase exponents of the stimulus phasor $A_{2,1}$. The parameter 'r' acts as the magnitude indexing term, generally limited to a maximum of $r_{\max} = 1$. Similarly, x defines the magnitude exponent of $|A_{1,1}|$, while 't' functions as the magnitude-restricting term for

$|A_{1,1}|$, typically varying between 0 and $t_{max} = 1$ in practical scenarios.

The parameter 'w', referred to as the '*mixing order*', defines the complexity of the Cardiff model and the highest order of terms it incorporates. For example, a Cardiff model with '$w = 3$' at the fundamental frequency includes terms up to the third order, while higher-order terms are excluded. In contrast, increasing the mixing order to '$w = 5$' allows the model to incorporate terms up to the fifth order, leading to a more intricate model with additional terms. According to the principles of mixing theory, it is typically advised to use an odd mixing order (e.g., 'w' as an odd number) for odd harmonics, such as the fundamental and third harmonic. Table. 3.1 outlines the order of model terms for a 5^{th}-order Cardiff model at the fundamental frequency ($h = 1$).

BIBLIOGRAPHY

[1] M. Golio, R. Trew, J. Golio, M. Steer, L. P. Dunleavy, C. Nelson, R. Newgard, R. E. Ham, W. R. Curtice, A. Parker, *et al.*, *RF and microwave circuits, measurements, and modeling*. CRC press, 2018.

[2] S. C. Cripps *et al.*, *RF power amplifiers for wireless communications*, vol. 250. Artech house Norwood, MA, 2006.

[3] V. Teppati, A. Ferrero, and M. Sayed, *Modern RF and microwave measurement techniques*. Cambridge University Press, 2013.

[4] D. M. Pozar, *Microwave and RF design of wireless systems*. John Wiley & Sons, 2000.

[5] F. M. Ghannouchi and M. S. Hashmi, *Load-pull techniques with applications to power amplifier design*, vol. 32. Springer Science & Business Media, 2012.

[6] M. S. Hashmi, F. M. Ghannouchi, P. J. Tasker, and K. Rawat, "Highly reflective load-pull," *IEEE Microwave Magazine*, vol. 12, no. 4, pp. 96–107, 2011.

[7] J. F. Sevic, *The Load-Pull Method of RF and Microwave Power Amplifier Design*. John Wiley & Sons, 2020.

[8] M. Spirito, L. De Vreede, M. De Kok, M. Pelk, D. Hartskeerl, H. Jos, J. Mueller, and J. Burghartz, "A novel active harmonic load-pull setup for on-wafer device linearity characterization," in *2004 IEEE MTT-S International Microwave Symposium Digest (IEEE Cat. No. 04CH37535)*, vol. 2, pp. 1217–1220, IEEE, 2004.

[9] G. P. Bava, U. Pisani, and V. Pozzolo, "Active load technique for load-pull characterisation at microwave frequencies," *Electronics Letters*, vol. 18, pp. 178–180, 1982.

[10] V. Teppati, A. Ferrero, and U. Pisani, "Recent advances in real-time load-pull systems," *IEEE Transactions on Instrumentation and Measurement*, vol. 57, no. 11, pp. 2640–2646, 2008.

[11] J.-E. Muller and B. Gyselinckx, "Comparison of active versus passive on-wafer load-pull characterisation of microwave and mm-wave power devices," in *1994 IEEE MTT-S International Microwave Symposium Digest (Cat. No.94CH3389-4)*, pp. 1077–1080 vol.2, 1994.

[12] J. Verspecht, "Large-signal network analysis," *IEEE Microwave Magazine*, vol. 6, no. 4, pp. 82–92, 2005.

[13] J. Verspecht, F. Verbeyst, and M. vanden Bossche, "Network analysis beyond s-parameters: Characterizing and modeling component behaviour under modulated large-signal operating conditions," in *56th ARFTG Conference Digest*, vol. 38, pp. 1–4, 2000.

[14] J. Benedikt, R. Gaddi, P. Tasker, and M. Goss, "High-power time-domain measurement system with active harmonic load-pull for high-efficiency base-station amplifier design," *IEEE Transactions on Microwave Theory and Techniques*, vol. 48, no. 12, pp. 2617–2624, 2000.

[15] R. S. Saini, S. Woodington, J. Lees, J. Benedikt, and P. J. Tasker, "An intelligence driven active loadpull system," in *75th ARFTG Microwave Measurement Conference*, pp. 1–4, 2010.

[16] J. Bardeen and W. H. Brattain, "Physical principles involved in transistor action," *Phys. Rev.*, vol. 75, pp. 1208–1225, Apr 1949.

[17] C.-T. Sah and B. B. Jie, "A history of mos transistor compact modeling," *Proc. NSTI Nanotech 2005*, pp. 347–390, 2005.

[18] J. Pedro and S. Maas, "A comparative overview of microwave and wireless power-amplifier behavioral modeling approaches," *IEEE Transactions on Microwave Theory and Techniques*, vol. 53, no. 4, pp. 1150–1163, 2005.

[19] T. Gasseling, "Compact transistor models: The roadmap to first-pass amplifier design success," *Microwave Journal*, March 2012. Accessed: 2012-12-09.

[20] T. Gasseling, D. Barataud, S. Mons, J.-M. Nebus, J.-P. Villotte, J. J. Obregon, and R. Quéré, "Hot small-signal s-parameter measurements of power transistors operating under large-signal conditions in a load-pull environment for the study of nonlinear parametric interactions," *IEEE Transactions on microwave Theory and Techniques*, vol. 52, no. 3, pp. 805–812, 2004.

[21] J. Verspecht, M. vanden Bossche, and F. Verbeyst, "Characterizing components under large signal excitation: Defining sensible "large signal s-parameters"?!," in *49th ARFTG Conference Digest*, vol. 31, pp. 109–117, 1997.

[22] J. Verspecht, D. Barataud, J.-P. Teyssier, and J.-M. Nébus, "Hot s-parameter techniques: 6 = 4 + 2," in *2005 66th ARFTG Microwave Measurement Conference (ARFTG)*, pp. 1–9, 2005.

[23] Verspecht and D. Root, "Polyharmonic distortion modeling," *IEEE Microwave Magazine*, vol. 7, no. 3, pp. 44–57, 2006.

[24] J. Verspecht, "Describing functions can better model hard nonlinearities in the frequency domain than the volterra theory," *Annex Ph. D. thesis, Vrije Universiteit Brussel, Belgium*, 1995.

[25] J. Peyton Jones and S. Billings, "Describing functions, volterra series, and the analysis of non-linear systems in the frequency domain," *International Journal of Control*, vol. 53, no. 4, pp. 871–887, 1991.

[26] J. Verspecht and P. Van Esch, "Accurately characterizing hard nonlinear behavior of microwave components with the nonlinear network measurement system: Introducing

'nonlinear scattering functions'," in *Proceedings of the 5th International Workshop on Integrated Nonlinear Microwave and Millimeterwave Circuits*, pp. 17–26, Citeseer, 1998.

[27] J. Verspecht, D. Williams, D. Schreurs, K. Remley, and M. McKinley, "Linearization of large-signal scattering functions," *IEEE Transactions on Microwave Theory and Techniques*, vol. 53, no. 4, pp. 1369–1376, 2005.

[28] D. Root, J. Horn, L. Betts, C. Gillease, and J. Verspecht, "X-parameters: The new paradigm for measurement, modeling, and design of nonlinear rf and microwave components," *Microwave Engineering Europe*, vol. 12, p. 16, 2008.

[29] H. Qi, J. Benedikt, and P. Tasker, "Direct extraction of large-signal table-based behavioural models from time-domain voltage and current waveforms," in *High Frequency Postgraduate Student Colloquium, 2005*, pp. 25–28, 2005.

[30] H. Qi, J. Benedikt, and P. J. Tasker, "Nonlinear data utilization: From direct data lookup to behavioral modeling," *IEEE Transactions on Microwave Theory and Techniques*, vol. 57, no. 6, pp. 1425–1432, 2009.

[31] H. Qi, J. Benedikt, and P. Tasker, "A novel approach for effective import of nonlinear device characteristics into cad for large signal power amplifier design," in *2006 IEEE MTT-S International Microwave Symposium Digest*, pp. 477–480, 2006.

[32] S. Woodington, T. Williams, H. Qi, D. Williams, L. Pattison, A. Patterson, J. Lees, J. Benedikt, and P. J. Tasker, "A novel measurement based method enabling rapid extraction of a rf waveform look-up table based behavioral model," in *2008 IEEE MTT-S International Microwave Symposium Digest*, pp. 1453–1456, 2008.

[33] J. J. Bell, *Input Harmonic and Mixing Behavioural Model Analysis*. PhD thesis, Cardiff University, 2014.

[34] R. Saini, *Intelligence driven load-pull measurement strategies*. PhD thesis, Cardiff University, 2013.

[35] R. S. Saini, J. J. Bell, T. Williams, J. Lees, J. Benedikt, and P. J. Tasker, "Interpolation and extrapolation capabilities of non-linear behavioural models," in *78th ARFTG Microwave Measurement Conference*, pp. 1–4, 2011.

[36] K. Minghao, *Geometric and frequency scalable transistor behavioural model for MMIC design*. PhD thesis, Cardiff University, 2016.

[37] M. R. Moure, M. Casbon, M. Fernández-Barciela, and P. J. Tasker, "Direct extraction of an admittance domain behavioral model from large-signal load-pull measurements," in *2017 IEEE MTT-S International Microwave Symposium (IMS)*, pp. 1057–1060, IEEE, 2017.

[38] E. Azad, *Efficiency improvement in base station power amplifiers*. PhD thesis, Cardiff University, 2023.

CHAPTER 4

LOAD-PULL-DRIVEN BEHAVIOURAL MODEL OF HEMT-STRUCTURED MICROWAVE SWITCHING CELL

In preparation for developing a reflective tunable termination based on HEMT-structured active devices—a topic that will be extensively discussed in subsequent chapters - it is essential to accurately characterise the intrinsic properties of the active device serving as the switching cell within the network. The operational constraints of this switching cell will ultimately dictate critical performance parameters, including frequency range, power-handling capability, and insertion loss. Although LP has been identified as a promising approach for large-signal characterisation of PAs and transistors, to the best of the author's knowledge, no previous studies have been reported that specifically utilise LP techniques for investigating the behaviour of microwave switches.

This chapter is based on the work published in [1] and presents a practical implementation of LP measurements at S-band frequencies using an active load-pull setup applied to HEMT-structured microwave switches, operating without signal amplification. The extracted data is utilised in the subsequent sections to develop a behavioural model, covering the specified frequency range and measured power levels.

4.1 Characterisation of HEMT-structured Switching Cell

A group of microwave switches with HEMT-structured epilayers has been investigated. These devices were fabricated using GaN on SiC, a technology that provides significant advantages, making it highly suitable for high-frequency and high-power applications. GaN showcases exceptional electrical properties, including a wide bandgap and high breakdown voltage, enabling devices to operate at higher voltages [2]. SiC substrates bring additional benefits with their robust thermal stability and conductivity, significantly enhancing device reliability and performance under extreme conditions [3]. The HEMT structure, with its high electron mobility and low on-resistance, leads to faster switching speeds and higher power density [4].

The devices are constructed with a symmetric layout, a fixed gate length of 150 nm, and a diverse array of gate fingers, including 3, 5, 7, and 9. All devices were fabricated and supplied by WIN Semiconductors Corp. in two different gate widths of 50 and 100 µm. As depicted in Figure 4.1, the devices are connected to the ground through the gate resistance $\approx 40\,\mathrm{k\Omega}$. The RF pads are designed with a pitch of 150 µm and configured as microstrip launchers to facilitate on-wafer measurements using ground-signal-ground (GSG) probes. The gate configuration allows device biasing through the GSG probes, eliminating the need for additional needles to supply the gate.

To narrow down the candidates from the mentioned number of devices for further investigation, standard S-parameter measurements were performed to evaluate their frequency domain response in terms of insertion loss and isolation.

S-parameter measurements were conducted on-wafer using a thru-reflect-match (TRM) calibration to align the reference planes to the device level. Various voltages were examined, determining 0 V and 20 V as the optimal voltages for the OFF and ON states, respectively. As depicted in Figure 4.2, the smallest device (3F50) exhibits the highest insertion loss, as shown in Figure 4.2a. However, it achieves an isolation performance exceeding -20 dB, which is superior to that of the other samples, as illustrated in Figure 4.2b. In contrast, the

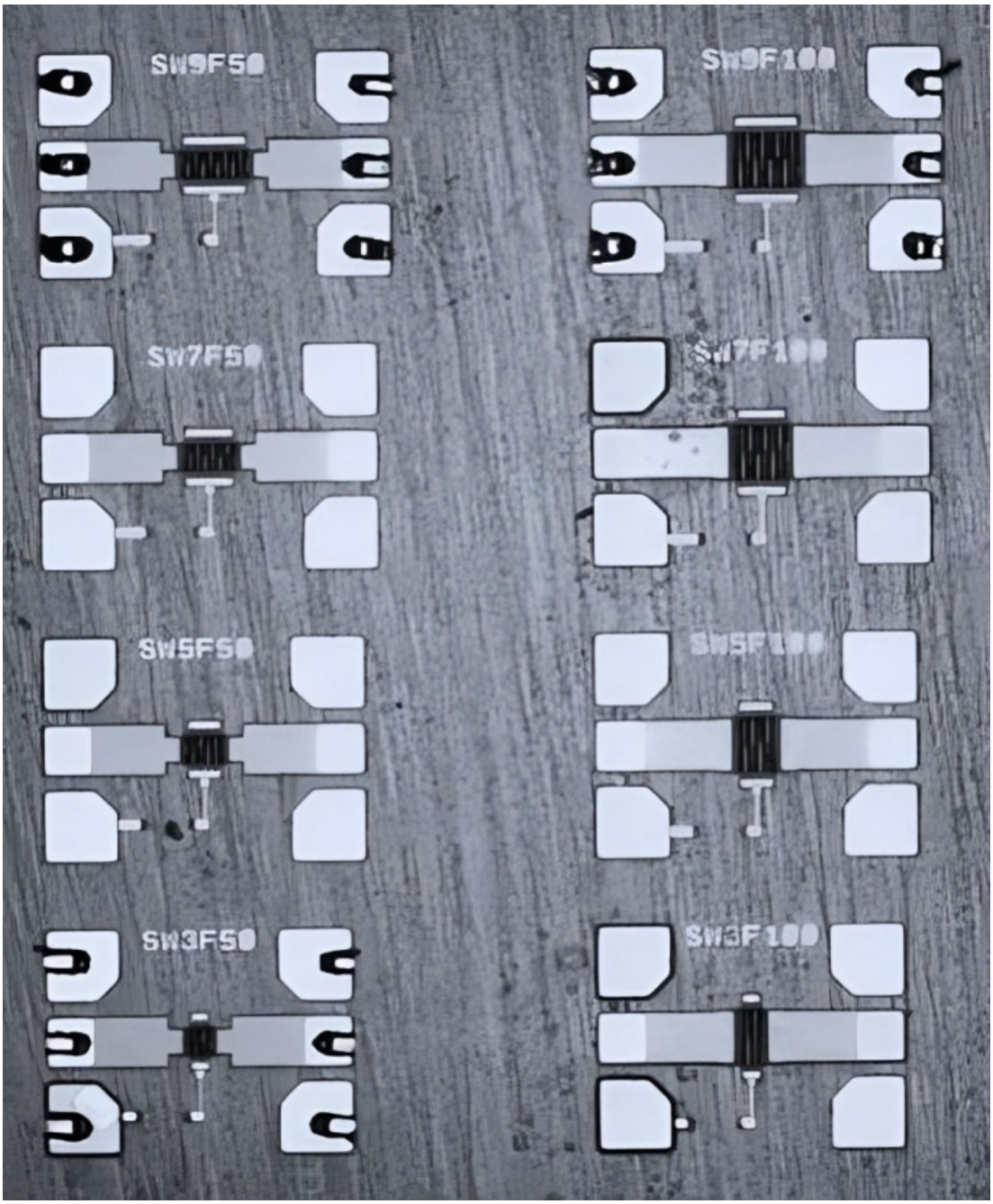

Figure 4.1: Microphotograph of the NP15 technology die fabricated by WIN Semiconductors Corp., the die includes eight unique samples with a fixed gate length of 150 nm and various gate finger configurations (3, 5, 7 and 9) with two gate widths of 50 and 100 µm.

largest device (9F100) displays opposing characteristics in both the ON and OFF states. This observation suggests that, depending on the design frequency and the desired trade-off between key FOM, such as isolation and insertion loss, the choice of channel periphery can be tailored to suit specific network requirements and applications.

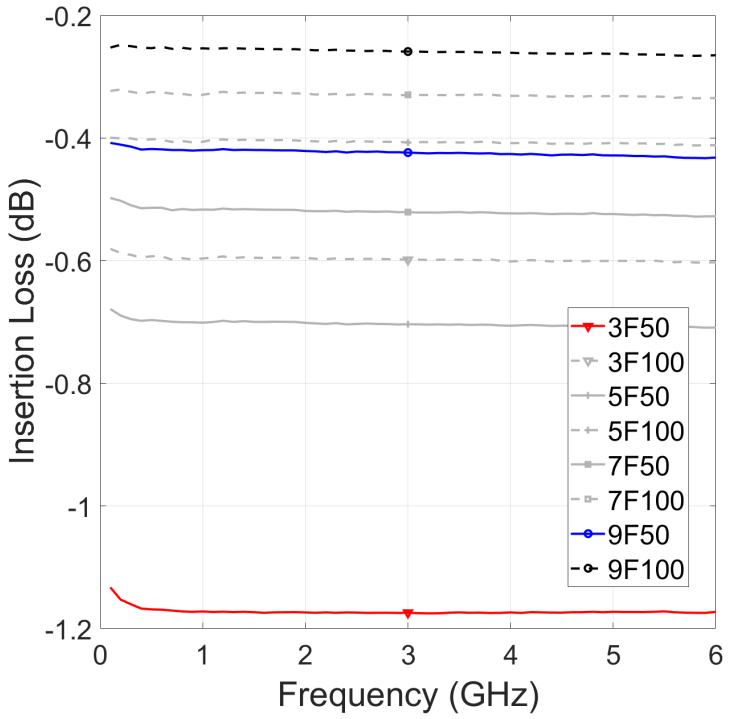

(a)

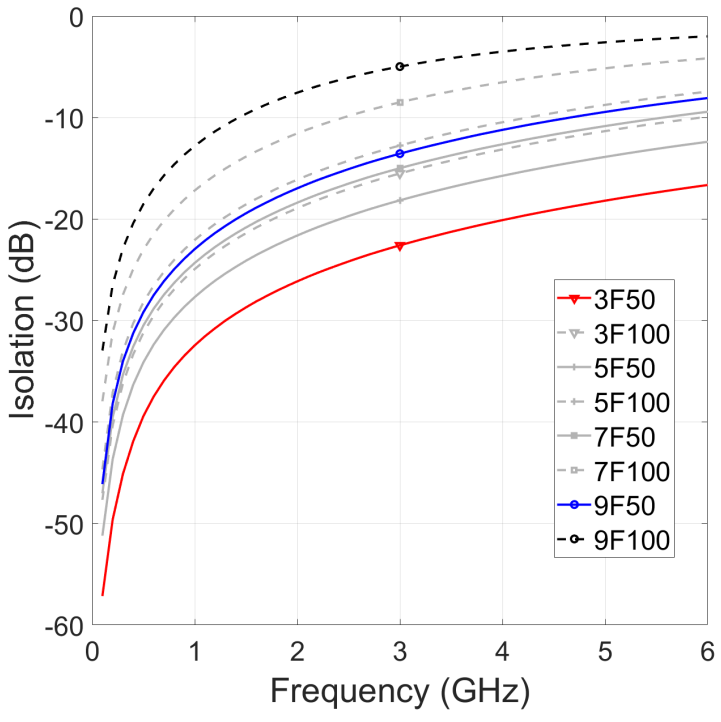

(b)

Figure 4.2: Frequency domain analysis of devices with various sizes. Insertion loss with 0 V applied to the gate as in on-mode (a) and isolation with negative 20 V as in off-mode (b) vs. frequency. Device size expressed as (number of fingers)F(gate width in µm).

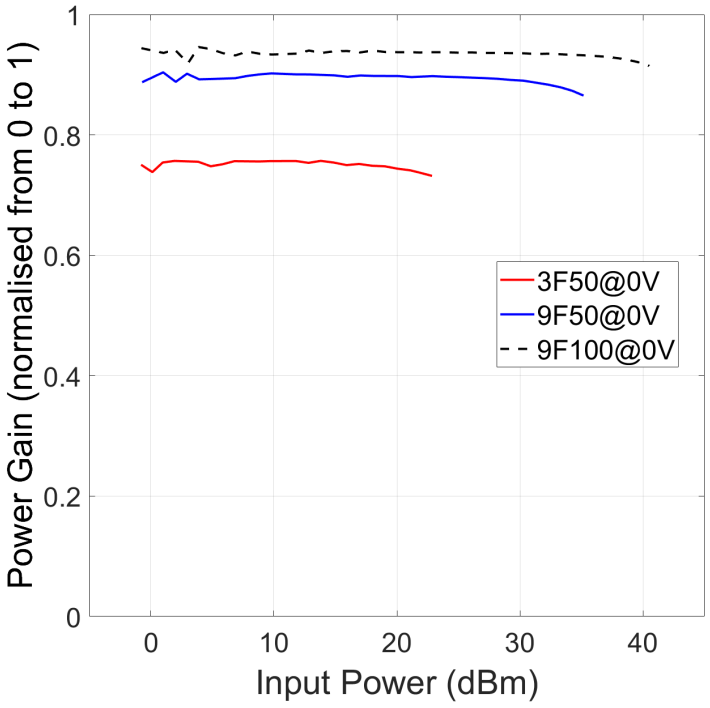

(a)

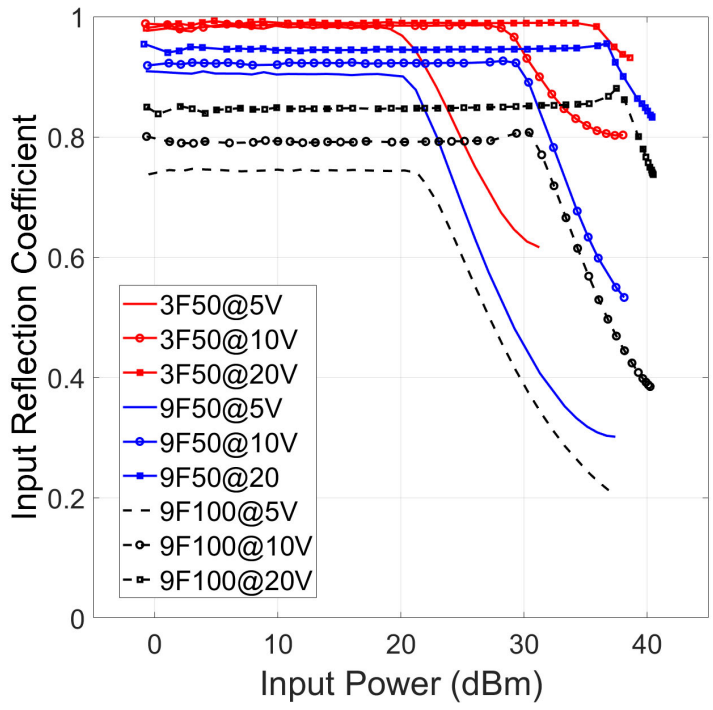

(b)

Figure 4.3: The power sweep illustration with 50 Ω condition at 3 GHz with CW excitation. The input power refers to the input reference plane of the switch. Insertion loss in on-mode (a); input reflection coefficient in off-mode (b).

Figure 4.3 illustrates the results obtained from standard 50 Ω power measurements under both ON and OFF conditions. The short listed devices, featuring periphery scaling factors of 1x (3F50), 3x (9F50), and 6x (9F100), were excited using a CW single-tone signal at 3 GHz. Figure 4.3a employs a linearised power gain, normalised to a range of 0 to 1, to characterise the associated losses of devices with varying aforementioned configurations in the ON state, biased at 0 V. In contrast, Figure 4.3b utilises the magnitude of the input reflection coefficients to evaluate isolation performance in the OFF state for same selected devices, biased at 5 V, 10 V, and 20 V.

Furthermore, Figure 4.3 provides insights into the power-handling capabilities of the devices relative to their size. In the ON state, the smallest device (3F50) exhibits compression onset at approximately 20 dBm of input power, whereas the largest device (9F100) shows only 0.1 dB of compression at 40 dBm input power. In the OFF state, the applied bias voltage is observed to be the dominant factor, surpassing the influence of device periphery. A bias voltage of 20 V demonstrates the highest power-handling capability across all device sizes, with the magnitude of the input reflection coefficient beginning to decline at input power levels of approximately 35-38 dBm for the tested devices.

Figure 4.4 depicts the progression of input reflection coefficients on the Smith Chart as the power level increases under off-state conditions. Transitioning from a lower off-state voltage of 5 V (Figure 4.4a) to a higher off-state voltage of 20 V (Figure 4.4c) reveals improved isolation, as evidenced by the input reflection coefficients more concentrated around the open point on the Smith chart. Furthermore, Figure 4.4 demonstrates that larger devices exhibit greater initial capacitance and lower reflectivity. It also highlights a phase shift occurring just prior to the onset of compression; this information could not be captured with a scalar 50 Ω measurement.

The LP measurement system used for this investigation is an open-loop active LP system, as shown in Figure 4.5. A Rohde and Schwarz ZVA67 VNA are employed to capture the calibrated a_i and b_i waves. The internal sources of the VNA are utilised to generate the input and load-pull signals, with the RF signals amplified by high-power driver amplifiers. To facilitate precise measurement of the fundamental frequency (F_0) at 3 GHz,

a bandpass filter was constructed by combining two 2–4.2 GHz filters with two 90-degree couplers. This configuration effectively isolates the desired signal by filtering out unwanted harmonics. The setup also incorporates bias-tees, which play a crucial role in enabling the feeding of terminals through GSG probes without the need for additional needles. Furthermore, two low-loss ultra-broadband directional couplers from Marki (C0265) are positioned at the input and output, just before the GSG probes.

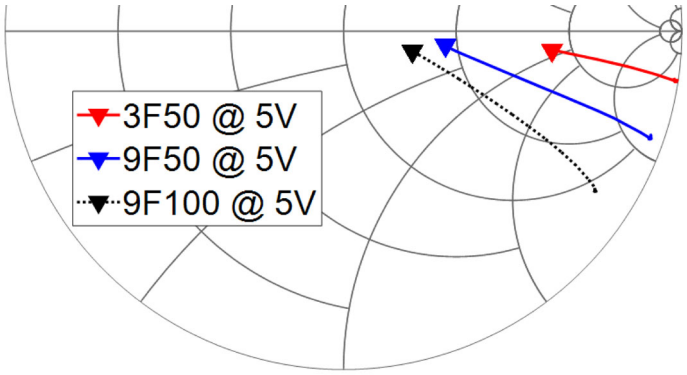

(a)

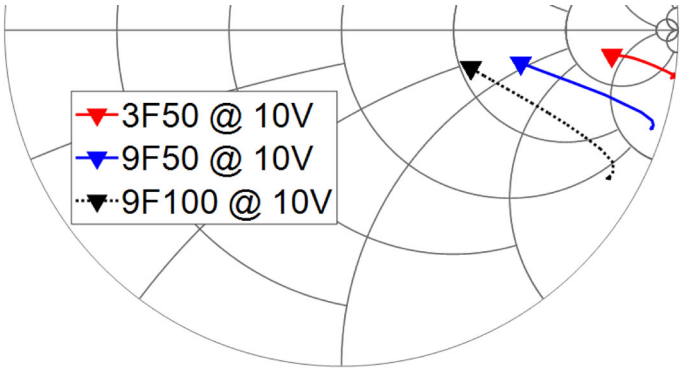

(b)

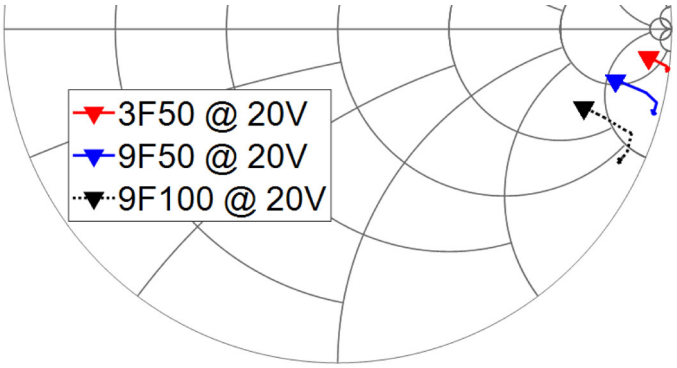

(c)

Figure 4.4: Input reflection coefficient (Γ_{IN}) vs. input power analysis of different device periphery at 3 GHz in different biasing in off-condition; at 5 V (a), 10 V (b), 20 V (c).

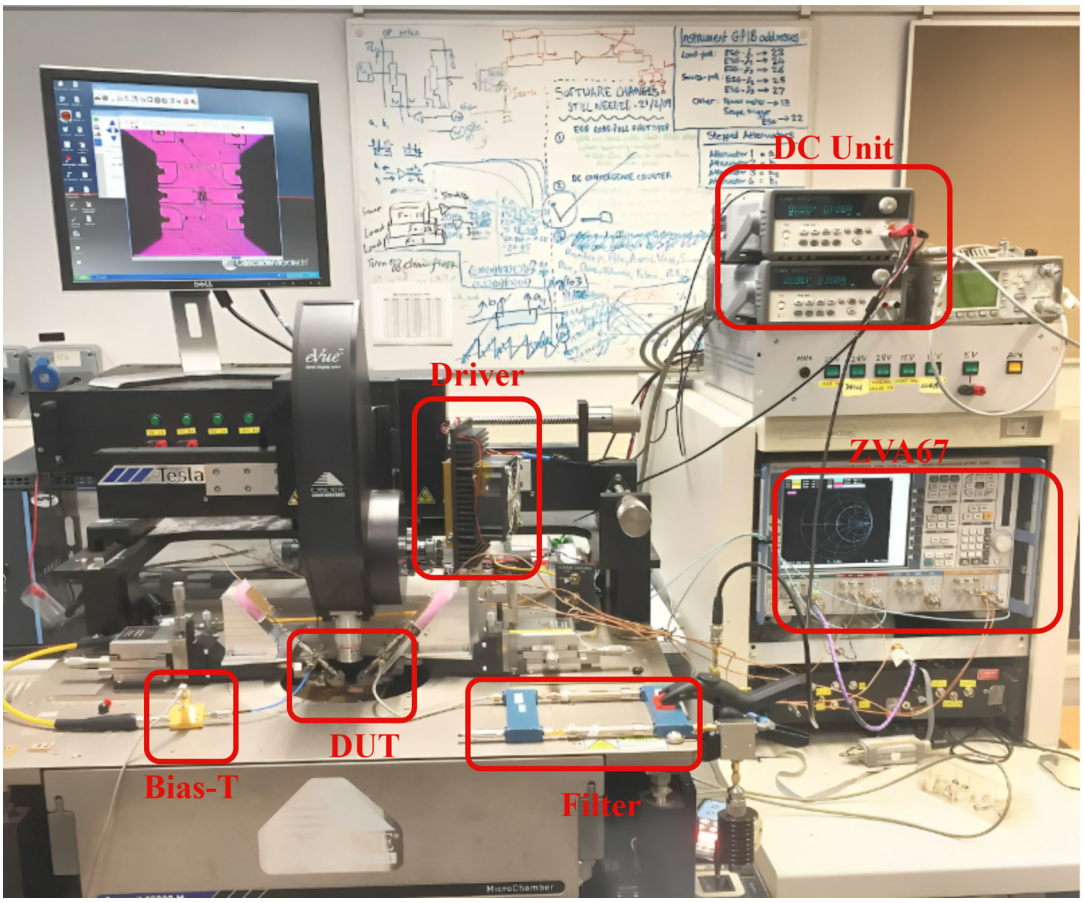

(a)

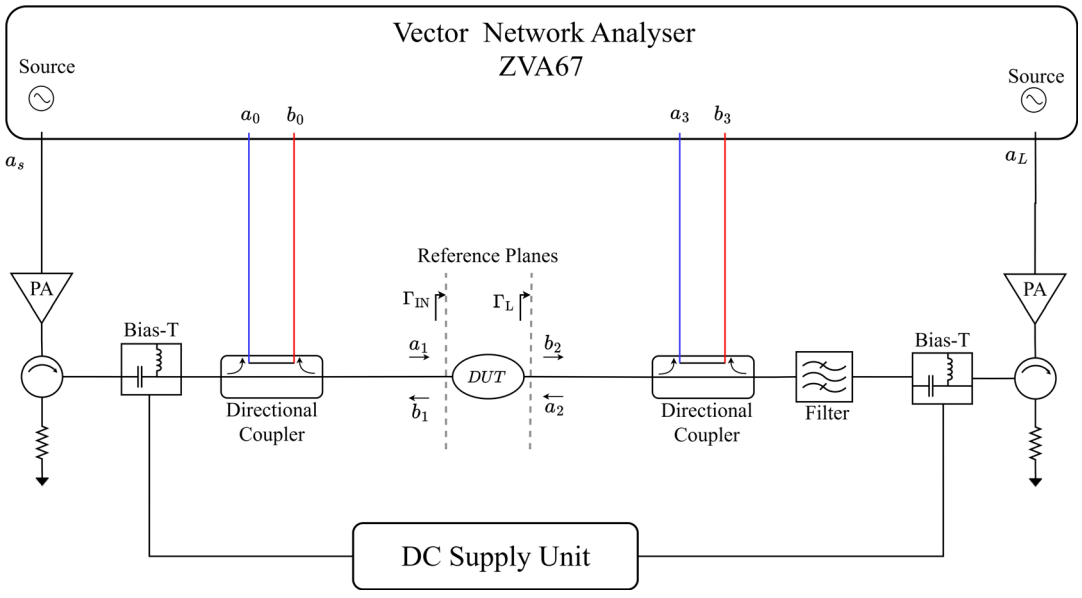

(b)

Figure 4.5: Active open-loop load-pull measurement system set up at Cardiff University to perform CW signal at 3 GHz (a); block diagram of the same system (b).

Figure 4.6 illustrates the load-pull measurement results for the 9F100 device under ON (Figure 4.6a) and OFF (Figure 4.6b) conditions at two distinct drive levels. These drive levels are determined from the 50 Ω power sweeps for each ON and OFF condition. The first power level indicates where the devices demonstrate linear behaviour, while the second corresponds to the 1 dB compression point. LP measurements were conducted at these selected power levels, capturing the input reflection coefficient (Γ_{IN}) responses. Γ_{IN} at linear power levels are marked by blue triangles, while Γ_{IN} at compressed power levels are marked by red triangles in both ON and OFF conditions. Black' x's indicate the load reflection coefficient (Γ_L) targeted for testing.

In the on-condition, compression reduces the coverage of the Smith Chart, particularly from the left-hand side, due to the dominant parasitic being the ON resistance, magnified when the devices are introduced to lower impedances. This effect is more substantial in compression (red triangles), indicating that the main consequence of compression is an increase in the equivalent ON resistance in the switch. In the off-condition, the input reflection coefficient is less dependent on the load due to isolation. However, non-perfect isolation leads to a pulling of the input impedance, which becomes more extensive in compression when the isolation is compromised.

Upon analysing the 3F50 device presented in Figure 4.7, it is evident that the input reflection coefficients (Γ_{IN}) exhibit greater deviation from the predefined load conditions in both linear and compressed drive levels compared to the 9F100 device shown in Figure 4.6b. This discrepancy can be attributed to the channel periphery of the devices, which directly impacts the on-resistance. In devices with smaller channel dimensions, the on-resistance, which is inversely proportional to the channel area, becomes more significant, leading to increased insertion loss and, consequently, greater deviation in the ON state relative to larger devices.

When the devices are in the OFF state, the smaller-channel device exhibits superior isolation, as evident from the comparison between Figure 4.6b and Figure 4.7b.

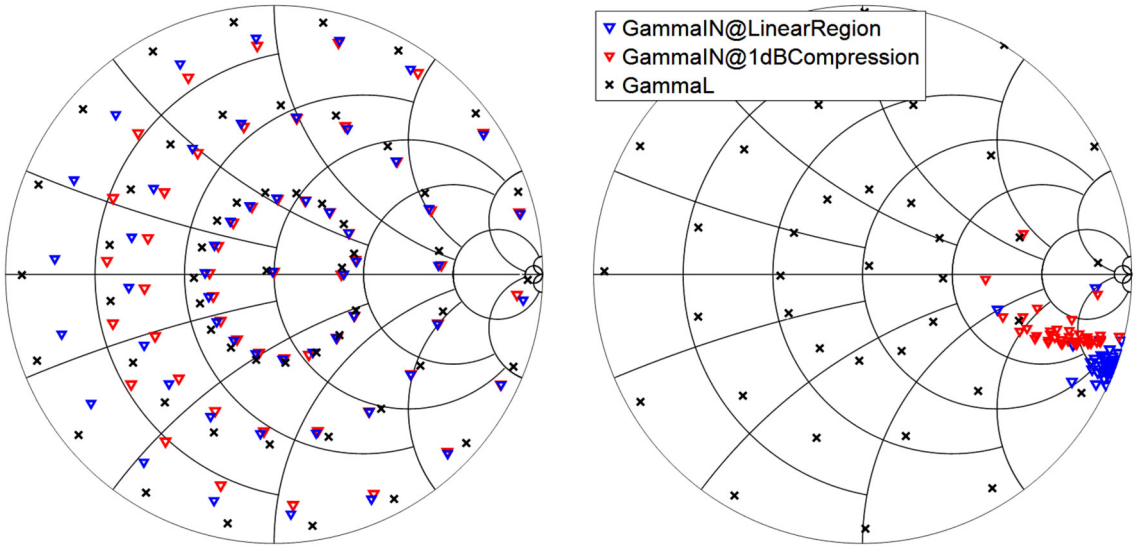

(a) (b)

Figure 4.6: The 9F100 device and its LP measurement results at 3 GHz. Defined output reflection coefficients (Γ_L) are shown in black 'x's, captured input reflection coefficients (Γ_{IN}) are shown in triangles with drive levels of linear region (blue) and 1 dB compression (red); ON condition (a), OFF condition (b).

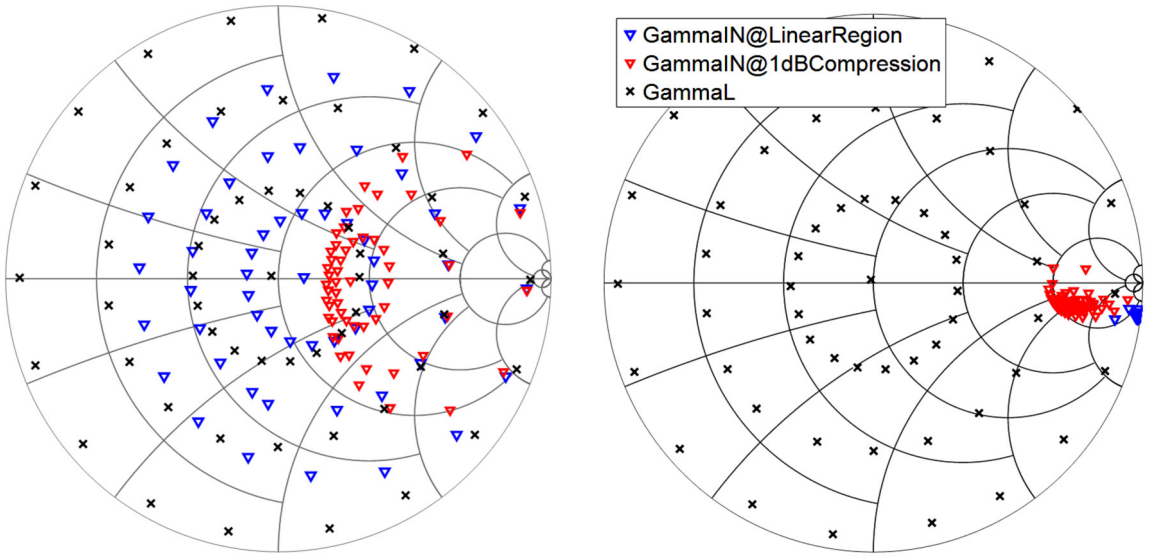

(a) (b)

Figure 4.7: The 3F50 device and its LP measurement results at 3 GHz. Defined output reflection coefficients (Γ_L) are shown in black 'x's, captured input reflection coefficients (Γ_{IN}) are shown in triangles with drive levels of linear region (blue) and 1 dB compression (red); ON condition (a), OFF condition (b).

4.2 Cardiff Behavioural Model

The experimental findings have revealed that the switch's response under compression is complex, with combined phase and magnitude deviations from the linear response. The Cardiff behavioural model [5] can be utilised to incorporate the measured load-pull data into a CAD software environment. This model mathematically represents the non-linear relationship between incident waves "A" and reflected waves "B" at the DUT plane:

$$B_{p,h} = (\angle A_{1,1})^h \sum_{r=0}^{1} \sum_{n=n_{\min}}^{n_{\max}} K_{p,h,m,n} |A_{2,1}|^m \left(\frac{\angle A_{2,1}}{\angle A_{1,1}}\right)^n \tag{4.1}$$

$$\begin{cases} n_{\min} = -\left(\dfrac{w-h}{2} - r\right) \\ n_{\max} = h + \left(\dfrac{w-h}{2} - r\right) \\ m = |n| + 2r \end{cases}$$

In Equation 4.1, "p" and "h" are port and harmonic indexes, respectively; "m" and "n" are ($A_{2,1}$) magnitude and phase exponents, while the magnitude indexing is represented by the term "r" which has a maximum value of "1." The model order "w" defines the complexity of the model. The model extraction process involves the identification of the coefficients "K" and can be easily performed with a least mean square algorithm.

Since the Cardiff model has been used almost exclusively to model transistors in active mode, in the case of switch modelling, to determine the appropriate model complexity for the highest achievable model accuracy, the model complexity (w) of 3, 5, and 7 are assessed through normalised mean squared error (NMSE), which is a figure of merit to calculate the overall deviation of the measurement and predicted data. The equation below illustrates the definition of NMSE.

$$NMSE = \frac{1}{N} \sum_{i} \frac{(P_i - M_i)^2}{\overline{P}\,\overline{M}} \tag{4.2}$$

$$\overline{P} = \frac{1}{N}\sum_{i} P_i \tag{4.3}$$

$$\overline{M} = \frac{1}{N}\sum_{i} M_i \tag{4.4}$$

Where "M" and "P" represent the measured and predicted (or modelled) data, respectively. The letter 'N' represents the number of loads measured during the load-pull measurement. Figure 4.8 presents the NMSE comparison of B1 and B2 components across different model orders under both ON and OFF conditions for the 3F50 and 9F100 devices. While the 7th-order model exhibits the lowest NMSE, the 5th-order model also demonstrates excellent accuracy. Given that the 5th-order model provides a favourable balance between computational efficiency and predictive accuracy, it is selected for the final model development.

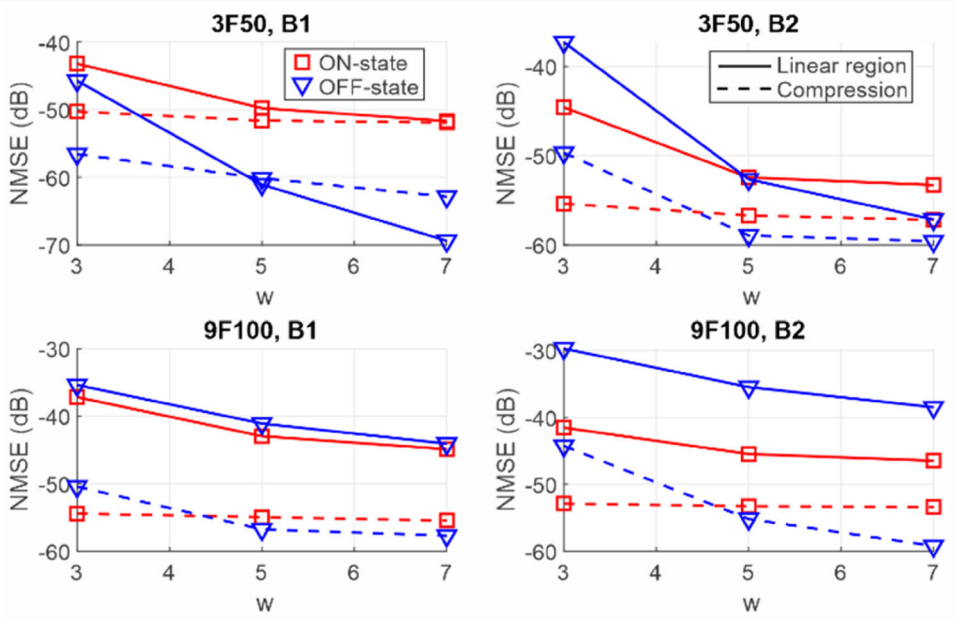

Figure 4.8: NMSE vs. model order for modelling B1 and B2 in both ON and OFF conditions at different drive levels

n	-2	-1	0	1	2	3	-1	0	1	2
m	2	1	0	1	2	3	3	2	3	4
r	0	0	0	0	0	0	1	1	1	1

Table 4.1: Exponent table to show case the coefficients for a model order of 5th.